How lipid composition shapes the nanostructural interaction of tumor biomarker alpha-fetoprotein and bovine serum albumin with model membranes

Beatrice Barletti, Melanie König, Nicoló Paracini, Giovanna Fragneto, Jean-Pierre Alcaraz, Andrew Nelson, Isabelle Vilgrain, Donald K Martin, Fabio Lolicato, Marco Maccarini

Journal of Colloid and Interface Science 708 (2026) 139753

Contents lists available at ScienceDirect

Journal of Colloid And Interface Science

journal homepage: www.elsevier.com/locate/jcis

How lipid composition shapes the nanostructural interaction of tumor biomarker alpha-fetoprotein and bovine serum albumin with model membranes

Beatrice Barletti [a,b], Melanie König [c], Nicoló Paracini [d], Giovanna Fragneto [d], Jean-Pierre Alcaraz [e], Andrew Nelson [f], Isabelle Vilgrain [g], Donald K. Martin [a], Fabio Lolicato [c,h], Marco Maccarini [a,*]

[a] Université Grenoble-Alpes, CNRS, Grenoble INP, LMGP-UMR 5628, 38000, Grenoble, France
[b] Institut Laue-Langevin, 38042, Grenoble, France
[c] Heidelberg University Biochemistry Center, Heidelberg, Germany
[d] European Spallation Source ERIC, P.O. Box 176, SE-221 00, Lund, Sweden
[e] Université Grenoble-Alpes, CNRS, Grenoble INP, TIMC/PRETA (UMR 5525), 38000, Grenoble, France
[f] Australian Nuclear Science and Technology Organisation (ANSTO), Sydney, New Illawarra Rd, Lucas Heights NSW 2234, Sydney, Australia
[g] Université Grenoble-Alpes, INSERM U13, CEA, Institute of Interdisciplinary Research of Grenoble (IRIG), Laboratory of Biosciences and Bioengineering for Health (BGE)-BIOMICS, 38054, Grenoble, France
[h] Department of Physics, University of Helsinki, Helsinki, Finland

ARTICLE INFO

Keywords:
Alpha-fetoprotein
Protein biomarkers
Lipid bilayers
Neutron reflectometry
Molecular dynamic simulations

ABSTRACT

This study systematically investigated the interactions of the tumor biomarker alpha-fetoprotein (AFP) and bovine serum albumin (BSA) with planar lipid membranes using neutron reflectometry, quartz crystal microbalance with dissipation monitoring, and atomistic molecular dynamics simulations. By examining a range of lipid compositions-including charged, neutral, and nanodomain-containing bilayers-we dissected the molecular mechanisms governing protein-membrane interactions. AFP consistently exhibited stronger interactions than BSA. While both proteins showed negligible binding to zwitterionic POPC bilayers, BSA only interacted significantly with negatively charged POPS membranes. In contrast, AFP strongly engaged with both SM/CHOL nanodomains and POPS-containing bilayers, leading to protein incorporation and lipid extraction, respectively. On positively charged DOTAP membranes, AFP formed a stable adsorbed layer. These findings reveal how lipid composition modulates protein adsorption, insertion, and membrane integrity, offering new mechanistic insights into the differential binding affinities of AFP and BSA. The results underscore the importance of protein-lipid interactions in clinical assays for blood tumor biomarkers, as these interactions may influence the formation of protein-lipid complexes and impact detection accuracy. This work may guide the optimization of biosensing strategies, particularly for glycosylated biomarkers, to enhance the sensitivity and reliability of clinical diagnostics.

1. Introduction

The detection of blood biomarkers through traditional techniques presents many challenges, primarily due to their low abundance, the complexity of biological fluids, and the extent of their glycosylation or glycation. Biomarkers are typically present in blood at very low concentrations, often in the range of pico- or nanograms per milliliter [1]. Their detection from blood or serum is hampered by their formation of complexes with lipids and/or lipoproteins, which are structurally intricate particles composed of a core of cholesterol esters and triglycerides, surrounded by free cholesterol, phospholipids, and apolipoproteins [2]. The glycosylated state of biomarkers may play a role in recognition and in enhancing protein-lipid interactions, promoting the formation of these complexes [3]. This is particularly relevant in routine clinical practice for the detection of cancer biomarkers, since these tests do not typically require patient fasting. The amount of lipids and lipoproteins varies with food consumption, and it has been demonstrated that biomarkers may become embedded within lipid particles (e.g., HDL and LDL particles)[3] rendering them undetectable through traditional techniques like Enzyme-Linked Immunosorbent Assay (ELISA) due to competing interactions between the assay and lipidic moieties present in the blood.

* Corresponding author.
E-mail addresses: fabio.lolicato@bzh.uni-heidelberg.de (F. Lolicato), marco.maccarini@univ-grenoble-alpes.fr (M. Maccarini).

https://doi.org/10.1016/j.jcis.2025.139753
Received 4 November 2025; Received in revised form 12 December 2025; Accepted 21 December 2025
Available online 1 January 2026

Previous studies have shown that glycosylated proteins such as CLA-1, Calvo et al. [4] CD36, Park [5], Rigotti et al. [6] and Hepatitis C virus glycoprotein E2, Cocquerel et al. [7], Bartosch et al. [8] interact with lipoproteins. A recent study demonstrated for the first time the direct interaction between the glycosylated biomarker, soluble Vascular-Endothelial cadherin (sVE), and HDL particles, suggesting that protein-lipid interactions contribute to the variability in biomarker detection [3]. However, the nanostructural mechanisms underlying these interactions remain poorly understood, particularly for specific cancer biomarkers. Understanding protein biomarker-lipid interactions is crucial not only for advancing fundamental knowledge but also for optimising the sensitivity and reliability of biosensing techniques used to identify protein biomarkers in blood samples, particularly when these proteins are glycosylated and challenging to detect with current methods. Additionally, lipids have the potential to serve as an effective platform for the development of innovative analytical and biosensing approaches [9–11].

Here, we focus on alpha-fetoprotein (AFP), a glycosylated biomarker associated with the development of liver cancer. AFP is a 69 kDa N-linked glycoprotein found in fetal serum, but its content is rapidly reduced in adults, reaching values that typically fall into the range of 5–10 ng/mL [12–14]. On the other hand, AFP concentration in serum increases in hepatocellular carcinoma (HCC) and other liver diseases, and its detection can anticipate tumor reappearance. Studies have shown that an AFP concentration above 400 ng/mL can generally be considered a diagnostic tool for HCC high-risk patients, [14] or consistently associated with poor prognosis in several treatments of HCC [15]. However, AFP has poor sensitivity and specificity, Piñero et al. [16] and levels below 100 ng/mL are less specific since similar values can also be found in patients with chronic hepatitis [17]. Despite this, the protein is still considered and used as a tumor-associated biomarker for HCC.

In this study, we investigate the nanostructural interaction between the glycosylated biomarker AFP and model cell membranes, with particular attention to how different lipid compositions modulate this interaction. The structural characterisation is performed using neutron reflectometry (NR) and quartz crystal microbalance with dissipation monitoring (QCM-D) on planar lipid bilayers. To establish a reference point for AFP-membrane interactions, we compare its behaviour with that of bovine serum albumin (BSA), a widely used model protein selected for its structural similarity to human serum albumin (HSA) and its ready commercial availability.

BSA has a molecular weight of approximately 66.5 kDa and is comprised of 583 amino acids arranged into three homologous domains, giving it an overall ellipsoidal shape. Its theoretical isoelectric point (pI) of 5.6 results in a net negative charge at physiological pH. The solution properties of BSA have been well characterized, with a reported monomeric gyration radius of 27.6Å [18]. Although albumins, including BSA, have traditionally been considered non-glycosylated, recent evidence suggests that low levels of glycosylation may occur at non-canonical sites [19]. Moreover, BSA contains residues susceptible to glycation, including lysine, arginine, and cysteine [20] and is well known for its multiple fatty acid (FA)-binding sites. While BSA is known to bind lipophilic compounds, its interactions with zwitterionic supported lipid bilayers are generally weak, although they may vary depending on the specific lipid composition. Previous studies have shown that BSA binds more strongly to charged lipids compared to zwitterionic lipids [21–23].

AFP is structurally related to albumin, containing approximately 585 amino acid residues organised into three homologous domains. Domain III at the C-terminus is the most conserved, while Domain I at the N-terminus shows more structural variation [24,25]. AFP adopts an asymmetric, heart-shaped conformation with dimensions of 93.2 Å x 83.3 Å x 59.6 Å, contains four natural FA-binding sites, and is N-glycosylated at residue N251 [25]. Structural studies combining electron density map and LC-MS/MS have provided insight into its glycan composition, including the mutant N251S [25]. The external surface of AFP is predominantly hydrophilic, favoring solubility in the bloodstream, whereas the FA-binding sites are lined by hydrophobic residues and flanked by positively charged side chains, particularly arginine and lysine [26,27]. Similar to BSA, AFP has a low theoretical pI (5.48), conferring a net negative charge at physiological pH. Given its comparable size and shape to BSA, we assume a similar gyration radius for AFP in this study.

To support the interpretation of the experimental results, we performed fully atomistic molecular dynamics (MD) simulations of AFP and BSA interacting with in silico-generated lipid bilayers that matched the experimental lipid compositions, for a cumulative simulation time of 40 microseconds. These simulations provided atomic-level information into protein-lipid interactions and how they are influenced by lipid composition, thereby enhancing our understanding of the molecular details governing these interactions and their potential structural implications.

This strategy allowed us to systematically explore how distinct biophysical properties influence protein-lipid interactions. Moreover, our experimental results and MD simulations enhance our understanding of the interaction mechanisms between biomarkers and lipidic moieties, highlighting any specific or non-specific interactions that could also be leveraged for potential biosensor applications.

2. Materials and methods

2.1. Materials

Alpha-fetoprotein (AFP) solution (catalogue number 105-11, purity > 99% (SDS-PAGE)) was purchased from Lee Biosolutions (Maryland Heights, MO USA); Bovine Serum Albumin (BSA) was purchased from Sigma-Aldrich (Darmstadt, Germany) in the form of lyophilized powder product number A8806-1G (CAS 9048-46-8, purity ≥ 96% (agarose gel electrophoresis)); Tris buffered saline pH 7.6 buffer was prepared using the BioUltra tablets from Sigma-Aldrich (Darmstadt, Germany). 1-palmitoyl-2-oleoyl-glycero-3-phosphocholine ($C_{42}H_{82}NO_8P$, 16:0-18:1 PC, POPC, 760.076 g/mol, CAS: 26853-31-6, purity >99% (TLC)), 1-palmitoyl-2-oleoyl-sn-glycero-3-phospho-L-serine sodium salt ($C_{40}H_{75}NO_{10}PNa$, 16:0-18:1 PS, POPS, 783.988 g/mol, CAS: 321863-21-2, purity >99% (TLC)), 1,2-dioleoyl-3-trimethylammonium-propane chloride salt ($C_{42}H_{80}NO_4Cl$, 18:1 TAP, DOTAP, 698.542 g/mol, CAS: 132172-61-3, purity >99% (TLC)), brain porcine sphingomyelin ($C_{41}H_{83}N_2O_6P$, SM, 760.223 g/mol, CAS: 383907-91-3, purity >99% (TLC)) and ovine wool cholesterol ($C_{27}H_{46}O$, CHOL, 386.654 g/mol, CAS: 57-88-5, purity >98% (TLC)) for SLBs preparation was purchased from Avanti Polar Lipids (Alabaster, AL, USA). The TBS buffer for protein preparation and formation of supported lipid bilayer (SLB) was previously degassed in a bath sonicator and filtered to 0.2 μm.

2.2. Supported lipid bilayer preparation

SLBs were formed through vesicle fusion using lipid vesicles of different lipid compositions. The vesicles were produced from films composed of pure, binary, and tertiary lipid mixtures of POPC, POPC/POPS (8:2), POPC/DOTAP (7:3), and POPC/SM/CHOL (6:3:1). The chemical structures of the lipids and the reference ternary phase diagram are shown in Figure S4 of the SI. These films were prepared by combining stock chloroform solutions at 1 mg/mL of each component in the specified molar ratios. The solvent was evaporated using a gentle nitrogen stream, followed by overnight drying under vacuum. After complete evaporation of the solvent, the dried mixed films were resuspended in 50 mM TBS pH 7.6 for QCM-D experiments or milliQ H_2O for NR experiments, achieving a final lipid concentration of 0.1 and 0.2 mg/mL, respectively. To facilitate vesicle formation, the suspensions underwent bath sonication for 20 mins, followed by tip sonication on ice for 15 mins at 50% amplitude, with 5-second on/off pulses, resulting in vesicles of approximately 1000 Å in diameter. For NR experiments, SLB formation was achieved via spontaneous vesicle fusion. Immediately before injection, the sonicated lipid suspension was mixed 1:1 with a 4 mM solution of $CaCl_2$, yielding

a final concentration of 0.1 mg/mL lipids and 2 mM $CaCl_2$. In the case of QCM-D experiments, vesicle fusion was typically induced by osmotic shock using MilliQ H_2O. For these experiments, the tip-sonication time was reduced to 5–10 mins, and no ice bath was used.

2.3. Neutron reflectometry - Experimental

Time of flight Neutron reflectometry (NR) experiments were conducted on the FIGARO instrument [28] at the Institut Laue-Langevin (Grenoble, France) employing a vertical scattering geometry (horizontal sample plane) with a $\Delta q/q$ resolution of 7%. Two incident angles, 0.7° and 3.0°, were employed in the measurements, which were conducted over a wavelength range of 2–20 Å. This setup yields a usable Q-range from 0.009 $Å^{-1}$ to approximately 0.25 $Å^{-1}$, beyond which the signal is dominated by the sample background.

The experiments employed solid/liquid sample cells, developed at the Institut Laue-Langevin, comprising a poly(ether ether ketone) (PEEK) trough that held the sample surface against a liquid-filled compartment. The sample cells, with a volume of approximately 2 mL, were connected via inlet teflon tubing to an HPLC pump for automated solvent exchange. The temperature of the cell was regulated by means of a water circuit constructed into the cell holder connected to a temperature-controlled water bath. The substrates for SLB formation were silicon blocks of surface area of 8 × 5 cm^2 with a thickness of 15 mm, polished to a roughness of less than 5 Å. Silicon blocks were cleaned by sonication in a series of solvents from apolar to polar for 20 mins. The solvents were, in order chloroform, acetone, ethanol and milliQ water. Crystals were then dried and placed in a UV/ozone cleaner for 30 mins, and then thoroughly rinsed with milliQ water. SLBs were formed on top of silicon blocks using the protocol described in Section 2.2 *Supported lipid bilayer preparation*. After the measurements of the pristine lipid bilayers, aliquots of proteins of 1.5 μM (around 0.1 mg/mL) were injected in the subphase and left incubating for a period of 5–7 h before rinsing with buffer solution. As reported in the Introduction section, physiological AFP levels range from 5–10 ng/mL [13] in healthy adults, with concentrations reaching 400 ng/mL under pathological conditions [14]. In contrast, albumin is present in serum at much higher levels, approximately 35–50 g/L [29]. In our experiments, protein concentrations were selected to replicate the albumin reference conditions from our previous work [30], allowing a direct comparison between AFP and BSA under identical, controlled conditions.

Experiments were conducted on the same system using different isotopic compositions for the bulk subphase. Mixtures of H_2O and D_2O were used as contrast variation to measure as-formed SLBs and SLBs in presence of proteins: 100% D_2O, SLD = 6.36 × 10^{-6} $Å^{-2}$, 66% D_2O/34% H_2O, denoted 4-matched water (4MW) SLD = 4 × 10^{-6} $Å^{-2}$, 38% D_2O/62% H_2O, denoted silicon-matched water (SMW) SLD = 2.07 × 10^{-6} $Å^{-2}$ and 100% H_2O, SLD = -0.56 × 10^{-6} $Å^{-2}$, using three and four different isotopic contrasts to study the SLBs alone and SLBs with proteins respectively. The contrast variation method relies on the assumption that the principal nanostructural features of the sample remain unaltered with the change of the isotopic contrast. Conducting the measurements on the same system at different isotopic compositions provides additional data sets that highlight the scattering of chemically different structural components at the interface. Simultaneous co-refining of these data sets enhances the accuracy and reliability of the results during the fitting process [31]. After exposure of the SLBs to proteins, the water contrast (100% H_2O) was measured both before and after rinsing, to check for changes in the system due to the first rinsing and ensure that the different water contrasts represent the same experimental system.

In neutron reflectometry experiment, an incident neutron beam hits a planar surface elastically and the intensity of the specular reflected beam is recorded as a function of wavelength (λ) and angle (θ). The reflectivity, defined as the ratio between the intensity of the reflected and incident beam, is measured as a function of the perpendicular component of the momentum transfer, Q_z [32]. The momentum transfer is expressed as:

$$Q_z = k_{i\perp} - k_{f\perp} = 2k_{i\perp} = \frac{4\pi}{\lambda}\sin\theta \quad (1)$$

where λ is the wavelength of the incoming neutron beam and θ is the incident angle formed with the interface

The reflectivity depends on the thickness, roughness and SLD of the layers present at the interface, with the SLD defined as:

$$\rho = \sum_j b_j n_j \quad (2)$$

where n_j is the number density of the atomic nucleus j and b_j represents its coherent scattering length, an empirical quantity that has been established for most nuclei and quantifies the strength of the interaction between a neutron and an atom.

2.4. Neutron reflectometry - Data analysis and modeling

The analysis of neutron reflectometry data is often model-dependent and requires the selection of an appropriate model of the interface to accurately extract structural information and capture changes caused by the interaction with proteins. Here, the interface is modeled as a series of parallel layers, named *slabs*, each defined by its average SLD, thickness, volume fraction of intercalated liquid phase, and roughness. These model parameters are used to compute the reflectivity profile, which is then matched against the experimental reflectivities through a fitting procedure that minimizes the difference between model and data.

We tested different models against the reflectivity data obtained in the measurements. These models represent a series of possible structural configurations describing different scenarios from a complete absence of protein, to protein adsorption onto the SLB, to protein penetration into the SLB at different depths. In order to build these models, the experimental system was divided into a set of slabs sandwiched between two infinitely thick slabs representing the fronting (silicon substrate) and the backing (liquid phase) media. The number of slabs varies depending on the given model chosen to represent the data. The pristine SLB was represented by a set of five slabs, the native SiO_2 layer, the inner head region, the inner tail region, the outer tail region and the outer head region of the lipids sandwiched between the fronting and backing medium (Fig. 1A). The SLDs of the head and tail regions were calculated as linear combinations of the SLDs of the individual components, using values from the literature [33,34] and the RefNX database, and were then fixed to these calculated values. The SLB with an adsorbed layer of proteins was represented by adding an extra slab on top the SLB, having the SLD of the protein (Fig. 1B). In the models representing protein penetration in one or more slabs of the SLB, the layers containing both the lipid and the protein were considered a mixed slab with a SLD of the non-solvent components equal to a linear combination of the SLDs of the lipid and protein components, multiplied by their respective relative volume fraction (Fig. 1C-D). The total protein volume fraction was constrained to remain consistent across successive slabs within 1%, with the contribution of water within each slab included in the calculation but not directly constrained. This constraint was applied to ensure consistency in the protein volume fractions across successive protein-containing layers and assumes that the protein behaves like a rigid body. AFP contains flexible domains and a small glycosylation site. At the level of an individual protein, a uniform volume fraction distribution may indeed not be the most accurate representation across the mixed slabs. However, neutron reflectometry (NR) averages over macroscopic timescales and over thousands of proteins. In the case of globular proteins such as AFP and BSA, this ensemble averaging smooths out local structural heterogeneity, making a uniform distribution a reasonable approximation.

The SLD of the proteins was calculated based on the atomic composition of the protein and of the estimated volume of the amino acid

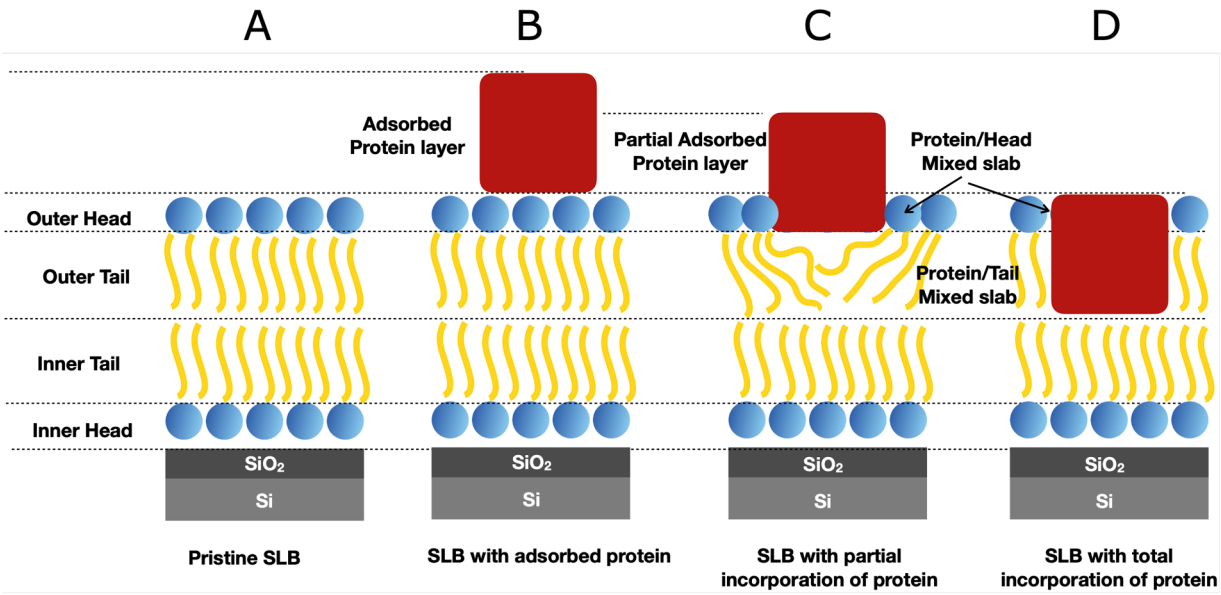

Fig. 1. Slab models used to build the model for the analysis of the reflectivity data. Reproduced with permission from reference [30].

using the Biomolecular Scattering Length Density Calculator [35]. The effect of D-H exchange of labile hydrogen atoms was included in the calculations.

The RefNX software [36] was employed for the analysis of the data. The data for each lipid bilayer was tested against the different models, which are depicted in Figure S1 of the Supporting Information. Reflectivity calculations employed the Abeles matrix formalism [37], incorporating interface roughness via the Nevot-Croce approach [38]. Uncertainties for the thickness, solvent volume fraction, and roughness of the lipid bilayers were determined from the posterior distribution of each parameter, obtained through Markov Chain Monte Carlo (MCMC) analysis. The corner plots generated from this analysis provide a visual representation of the parameter correlations and uncertainties. An example of a corner plot for a pristine lipid bilayer is shown in Figure S2 in the SI, illustrating the posterior distributions and confidence intervals for the relevant parameters.

The quality of the fitting and the most appropriate model were chosen based on the smaller normalised χ^2. In some cases, the choice of the best model was further guided by a critical analysis of the posterior distribution obtained by the Bayesian error analysis of some key parameters as described previously [30].

2.5. Quartz crystal microbalance with dissipation monitoring (QCM-D)

A Q-Sense E4 instrument (Q-sense, Biolin Scientific AB, Gothenburg, Sweden) was used to monitor in real time lipid and protein adsorption by measuring changes in resonance frequency and energy dissipation of silicon oxide-coated quartz crystals (QSX 303). QCM-D data were collected at the 3rd, 5th, 7th, 9th, and 11th odd overtones. The temperature was kept at 22°C during the whole measurement. Frequency shifts (Δf) indicate changes in the mass coupled to the sensor surface (analyte mass and hydrodynamically coupled water), whereas variations in energy dissipation shifts (ΔD) are associated with the viscoelastic properties of the system, providing quantitative information on the rigidity/softness of the adsorbed film [39].

The QCM-D sensor crystals were cleaned by bath-sonication in different solvents from apolar to polar (chloroform, acetone, ethanol and ultrapure Milli Q water) for 10 mins each, followed by drying with nitrogen stream and treatment with UV/ozone cleaner (BioForce Nanosciences, Inc., Ames, IA) for 30 mins and thorough rinsing in Milli Q to remove organic material and render the surface hydrophilic.

SLBs were prepared through the fusion of lipid vesicles formed from different lipid compositions. The fusion process was followed by monitoring Δf and ΔD overtones, until constant values were reached that indicated formation of a complete bilayer. The formation of a SLB has a characteristic signature in the time-evolution of the QCM frequency and dissipation as displayed in Figure S3. First, adsorption of intact vesicles on the quartz surface causes a decrease in the frequency, accompanied by an increase in the dissipation. When the frequency shift reaches approximately -60 Hz and the dissipation is 5 ppm, vesicles reach the maximum crowding on the surface and coalesce into a lipid bilayer. This causes the release of water trapped in the vesicles, which translates into a stabilisation of the frequency signal around -25 Hz. The difference between the initial and the final values of frequency and dissipation is related to the characteristics of the sample formed. For example, values of frequency and dissipation shifts indicating formation of a complete supported lipid bilayer of POPC are $\Delta f \sim$ -26 Hz and $\Delta D \sim 0.2 \times 10^{-6}$ [40,41]. Aliquots of protein solutions at 1.5 μM were sequentially added to the SLB-coated QCM-D sensor while monitoring Δf and ΔD overtones. All QCM-D experiments were performed in triplicate.

Relative frequency values relevant for the interpretation of the data are reported for the pristine bilayer (f_1), the bilayer in the presence of the protein (f_2), the bilayer in the presence of the protein after the incubation period (f_3) and the bilayer after rinsing away the protein with buffer (f_4). To assess whether the addition of the protein causes an increase in mass (adsorption) or a decrease in the mass (desorption) of the system, ΔF_a and ΔF_b are defined.

$$\Delta F_a = f_2 - f_1 \tag{3}$$

$$\Delta F_b = f_4 - f_1 \tag{4}$$

Positive values of these parameters correspond to desorption processes, i.e., loss of material, while negative values correspond to adsorption processes in the system.

To estimate the changes in adsorbed surface mass (Δm) based on the observed frequency shift (Δf) the Sauerbrey equation can be used. This relation provides a good estimation of the mass of adlayers when the dissipation-to-frequency ratio is low ($\Delta D/\Delta f \leq 0.1 \times 10^{-6}\ Hz^{-1}$) [39]. The equation applies when the formed film is rigid, laterally homogeneous, and adsorbed rigidly onto the sensor surface. In QCM-D

experiments, these conditions are typically indicated by the overlap of all the frequency overtones and a ΔD value close to 0 for all the harmonics. The Sauerbrey equation is expressed as [42]:

$$\Delta m = -\frac{C \cdot \Delta f}{n} \tag{5}$$

where Δm is the mass change, Δf is the frequency shift expressed in absolute values, C is the mass sensitivity constant of the quartz crystal, which is dependent on the fundamental frequency and material properties (for standard quartz crystal with fundamental frequency of 5 MHz, $C = 17.7\,\mathrm{ng \cdot cm^{-2} \cdot Hz^{-1}}$), n is the overtone number ($n = 1, 3, 5, \ldots$).

Mass changes at the sensor surface for the different SLBs were calculated both after the addition of proteins (defined as Δm_a) and after long exposure to proteins and rinsing with buffer (defined as Δm_b). Δm_a and Δm_b are calculated from absolute values of ΔF_a and ΔF_b respectively using the Sauerbrey equation. In our experiments, the conditions for applying the Sauerbrey equation were fulfilled for the pristine SLBs and the SLBs exposed to proteins after rinsing with the buffer. While, as it will be discussed in the results section, for the calculation of Δm_a the use of the Sauerbrey equation is an approximation since the overtones are not overlapping and the dissipation is not negligible. The software Qsoft 401 v2.5.10 was used for data acquisition, while the data were analysed using Igor64 Pro-9 and Qtool.

2.6. Molecular dynamics simulations

All-atom molecular dynamics simulations were performed using GROMACS 2024 [43] with the CHARMM36m force field for proteins and lipids [44,45]. All systems were solvated with CHARMM-compatible TIP3P water and neutralised with potassium chloride using standard CHARMM ion parameters. The simulations were based on the crystallographic structure of bovine serum albumin (BSA; PDB 3v03 [46]) and the cryo-EM structure of human alpha-fetoprotein (AFP; PDB 7yim [47]). All termini were modeled as charged; AFP included a glycosylation at N251 with a core trisaccharide N-glycan (GlcNAcβ1–4GlcNAcβ1–4Manβ) linked via an N-glycosidic bond. The protein and membrane systems were built separately via the CHARMM-GUI web server [44], with membranes of 964 lipids in four compositions: POPC; POPC/POPS 8:2; POPC/DOTAP 7:3; and POPC/NSM/CHOL 6:3:1, where Nervonoyl-sphingomyelin (NSM) mimics porcine brain sphingomyelin used experimentally. Final systems were assembled by positioning the protein at a distance ≥ 20 Å from the membrane in 10 distinct orientations using an in-house script. Subsequently, each system was solvated, neutralised, and 150 mM KCl ions were added to mimic the experimental conditions. All systems were then energy-minimized and equilibrated using a six-step restraint-release protocol, followed by a 500 ns simulation. Temperature was maintained at 310 K using the V-rescale thermostat [48] with a coupling time of 1.0 ps. Pressure was kept at 1 atm using a semi-isotropic C-rescale barostat [49] with a time constant of 5.0 ps and an isothermal compressibility of 4.5×10^{-5} bar^{-1}. The Verlet cutoff scheme was used with a neighbor list update every 20 steps. Electrostatic interactions were calculated using the Particle Mesh Ewald (PME) method [50] with a real-space cutoff of 12 Å. Van der Waals interactions were treated with a force-switch modifier between 10 and 12 Å. Simulations were performed using a 2 fs integration time step and run for 500 ns per system, resulting in a cumulative simulation time of 40 µs. If not stated otherwise, the last 200 ns of each trajectory were used for analysis. All analyses were conducted using an in-house tool in combination with MDAnalysis [51] and lipyphilic [52].

2.6.1. Lipid depletion/enrichment around BSA and AFP

To quantify the local enrichment or depletion of lipid species around a protein, we compute the depletion/enrichment index (DEI) as:

$$\mathrm{DEI}_i = \frac{\rho_i^{\mathrm{contact}}}{\rho_i^{\mathrm{bulk}}} - 1 \tag{6}$$

where $\rho_i^{\mathrm{contact}}$ is the relative abundance (or normalized number density) of lipid species i in contact with the protein ρ_i^{bulk} is the corresponding abundance of lipid i in the bulk membrane.

2.6.2. Local lipid environment in POPC/NSM/CHOL membrane

A clear picture of the aggregation of certain lipid species can be gained by considering the enrichment/depletion index of each lipid species as described by Ingólfsson et al. [53]. In short, the lipid enrichment index of species B around species A, E_{AB}, may be defined as:

$$E_{AB} = \frac{N_{AB}}{\langle N_B \rangle} \tag{7}$$

where N_{AB} is the number of molecules of species B around species A, and $\langle N_B \rangle$ is the mean number of species B around any species.

3. Results

4. Mass adsorption/desorption analysis and viscoelastic properties using QCM-D

QCM-D allows the detection of real-time changes of surface-adsorbed materials in terms of mass and viscoelastic properties by monitoring the change in resonant frequency and energy dissipation occurring on a silicon oxide-coated quartz crystal on top of which the material is adsorbed. Hence, QCM-D can give insights into the formation of a SLB and into the balance of adsorption-desorption processes occurring on the SLB.

Reproducible SLBs for each of the four lipid compositions selected were obtained with this method. In the case of negatively charged and zwitterionic lipid compositions, SLBs formed through adsorbed vesicles rupture and fusion at a critical surface coverage level or induced by osmotic shock (Figure S5) [54,55]. The formation of SLB from the composition POPC/SM/CHOL 6:3:1 consistently showed higher values of frequency (~ -27 Hz) compared to the other compositions. This is in agreement with the presence of more densely packed lipids in the SLB due to the formation of SM- and CHOL-enriched domains. Due to the cationic character, POPC/DOTAP 7:3 vesicles did not accumulate on the sensor surface to the same extent as the other lipid compositions but initiated the fusion process earlier, as shown by the reduced vesicle adsorption peak compared to the other SLBs (see Figure S5D of the SI). In summary, all SLBs yielded Δf values between -24.3 Hz and -27.6 Hz.

Once the SLBs were formed, a protein solution of concentration around 0.1 mg/mL (1.5 μM) was introduced in the liquid sub-phase and left incubating for several hours (between 5 and 7 h). Examples of the effects of BSA and AFP additions for the pure POPC SLB are reported in Figure S6. After the incubation, the system was rinsed with buffer solution to remove the excess protein.

Table 1 shows frequency values of the pristine bilayer (f_1), the bilayer after the addition of the protein (f_2), the bilayer exposed to the protein after the long incubation period (f_3) and the bilayer exposed to the protein after rinsing with buffer (f_4) for all the lipid compositions. In addition, to facilitate the interpretation of the data, values of ΔF_a and ΔF_b are also shown (see Methods section).

In the case of BSA, the frequency/dissipation curves showed only minor changes after protein injection, as illustrated in Figure S7 of the SI. During the prolonged incubation period, the values of frequency and dissipation remained nearly stable and the rinsing with buffer caused negligible changes for most of the lipid compositions (close to the standard errors), with exception of POPC/DOTAP SLB, where a continuous

Table 1
Frequency shifts (7th overtone) of SLBs before and after the exposure to AFP and BSA proteins. The reported values are calculated as mean values between three repeated measurements and errors represent standard errors. Examples of the corresponding QCM-D experiments are shown in Fig. 7 and Fig. 2A–D. ΔF_a and ΔF_b are calculated according to equations reported in the method section.

Frequency shift (Hz)	AFP	BSA
POPC		
Pristine bilayer (f_1)	-24.3 ± 0.7	-24.9 ± 0.7
SLB + addition of protein (f_2)	-34.2 ± 1.0	-24.3 ± 0.5
SLB + protein after long incubation (f_3)	-32.7 ± 1.7	-23.9 ± 0.6
SLB + protein after rinsing with buffer (f_4)	-22.6 ± 1.2	-24.5 ± 0.6
$\Delta F_a = f_2 - f_1$	-9.9 ± 1.7	+0.6 ± 0.2
$\Delta F_b = f_4 - f_1$	+1.7 ± 1.0	+0.4 ± 0.4
POPC/SM/CHOL 6:3:1		
Pristine bilayer	-27.0 ± 0.7	-27.6 ± 0.2
SLB + addition of protein	-32.8 ± 0.4	-27.7 ± 0.3
SLB + protein after long incubation	-32.3 ± 0.5	-28.9 ± 0.9
SLB + protein after rinsing with buffer	-26.1 ± 0.6	-28.4 ± 0.6
ΔF_a	-5.8 ± 0.4	-0.1 ± 0.1
ΔF_b	+0.9 ± 0.1	-0.8 ± 0.4
POPC/POPS 8:2		
Pristine bilayer	-25.4 ± 1.0	-24.4 ± 1.3
SLB + addition of protein	-33.7 ± 1.4	-22.9 ± 1.0
SLB + protein after long incubation	-33.2 ± 1.4	-23.4 ± 2.0
SLB + protein after rinsing with buffer	-24.8 ± 0.9	-23.2 ± 2.0
ΔF_a	-8.3 ± 1.7	+1.5 ± 0.1
ΔF_b	+0.6 ± 0.1	+1.2 ± 0.7
POPC/DOTAP 7:3		
Pristine bilayer	-25.25 ± 0.04	-24.4 ± 0.6
SLB + addition of protein	-33.7 ± 1.5	-23.0 ± 0.5
SLB + protein after long incubation	-33.7 ± 0.6	-21.0 ± 0.5
SLB + protein after rinsing with buffer	-28.0 ± 0.4	-20.7 ± 0.5
ΔF_a	-8.4 ± 1.5	+0.6 ± 0.1
ΔF_b	-2.8 ± 0.4	+3.6 ± 0.1

increase in the frequency shift was observed throughout the incubation time, suggesting degradation of the bilayer due to removal of lipids (Figure S7D). An interesting behavior was also observed for the composition containing POPS (negatively charged lipid), in which the addition of BSA resulted in a slight increase in frequency (f_2 in Table 1), indicating the removal of lipids. However, this was followed by a subsequent decrease in frequency during the long incubation (f_3 in Table 1), suggesting the possible adsorption of BSA molecules onto the bilayer.

In contrast to BSA, the injection of AFP resulted in a significant decrease in frequency and an increase in dissipation for all lipid compositions (see Fig. 2A-D). The differences in frequency shift between pristine bilayers and bilayers exposed to AFP (defined as ΔF_a) are -9.9 Hz, -5.8 Hz, -8.3 Hz, and -8.4 Hz for POPC, POPC/SM/CHOL, POPC/POPS, and POPC/DOTAP, respectively (Table 1). These negative values of ΔF_a indicated a notable increase in mass at the sensor surface following injection of AFP. This suggests that, in the presence of excess protein, the interaction behavior was similar across all lipid compositions, with a small but detectable interaction of the protein with lipids. Moreover, Δf and ΔD corresponding to the different overtones were no longer superimposed, indicating the formation of a viscoelastic system, indicative of adsorption of a hydrated protein layer on the bilayer [56].

Conversely, the behaviour of the SLBs differed during the long incubation period and especially after the final rinsing with buffer, in which small but significant changes were specific to the different lipid composition of the SLBs. SLBs composed of POPC/SM/CHOL and POPC/POPS remained stable in terms of frequency and dissipation shifts during the long incubation (Fig. 2B and C), whereas the POPC SLB showed a minor increase in frequency of +1.7 ± 1.0 Hz, suggesting a possible removal of some of the lipids (Fig. 2A). By contrast, the SLB composed of POPC/DOTAP exhibited a decrease in frequency of -2.8 ± 0.4 Hz, suggesting the presence of stably adsorbed proteins (Fig. 2D).

At the end of the incubation period, the SLBs were rinsed with buffer solution to remove excess protein. In the case of AFP, the values of frequency and dissipation shifts increased and decreased, respectively, with rinsing for all the different compositions, reaching values similar to those of the pristine bilayers, indicating the washing away of the majority of proteins. Nevertheless, small but significant changes in frequency compared to the pristine bilayers (represented by ΔF_b) indicated that the interaction was not entirely reversible and affected the structure of bilayers. In addition, the rinsing with buffer restored the superimposition of Δf and ΔD overtones, indicating the return to a more rigid system, most likely removing excess proteins adsorbed onto the SLBs which formed more viscoelastic systems.

These changes were composition-dependent. For zwitterionic (POPC and POPC/SM/CHOL) and negatively charged (POPC/POPS) lipid compositions, frequencies reached a higher value compared to that of the pristine bilayer (positive ΔF_b values, Table 1) indicating mass loss on the SLBs due to a predominant removal of lipids. In contrast, for the cationic SLB with DOTAP the frequency value after rinsing was lower than that of the pristine bilayer (negative ΔF_b values, Table 1) indicating a positive mass gain (+47.1 ± 7.3 ng/cm^2) that could be attributed to the presence of residual adsorbed proteins on the bilayer. Interestingly, the same lipid composition exposed to BSA produced the opposite effect, with a mass loss of the SLB equal to -61.3 ± 1.7 ng/cm^2. These values were calculated using the Sauerbrey equation with ΔF_b in absolute value as explained in the Methods Section 2.5.

Mass changes at the sensor surface for the different SLBs following protein addition (Δm_a) and after prolonged exposure plus buffer rinsing (Δm_b) are represented in the histograms in Fig. 2E and F, respectively. Δm_a and Δm_b were calculated from the absolute values of ΔF_a and ΔF_b using the Sauerbrey equation. It should be noted that for the calculation of Δm_a, the use of the Sauerbrey equation is an approximation since the overtones were not overlapping and the dissipation was non-negligible. In this case, a viscoelastic model would be more appropriate for an accurate interpretation. However, given that the dissipation remained small, the Sauerbrey equation was applied to provide an approximate estimate of the mass.

These results indicate that, in the dilute concentration regime, AFP adsorbs on the membrane when the protein is in excess in the buffer, whereas BSA only induces minor changes. However, upon rinsing, the interpretation of QCM-D data becomes more complex. This is because the final frequency value (f_4) is the result of different contributions, namely the adsorption of proteins upon injection and incubation, the removal of lipids, and also the washing away of proteins after the rinsing. QCM-D experiments are valuable since they quantify the net mass balance (adsorption/desorption) occurring at the lipid bilayer upon interaction with the proteins. However, they are limited by the fact that they cannot distinguish between the contribution to the mass balance of the specific components (lipids and proteins). To overcome this limitation, we complemented the QCM-D experiments with neutron reflectometry, which can disentangle the structural contributions of proteins, lipids, and solvent.

5. Nanostructural characterisation with neutron reflectometry

Neutron reflectometry experiments were performed on the four supported lipid bilayers adsorbed on silicon blocks. The different SLBs were structurally characterised prior and after the exposure to the two proteins as described in the Methods Section 2.3.

After the exposure of the SLBs to AFP and BSA for a period of time between 5 and 7 h, the liquid phase was exchanged by flowing buffer solution for around 10 mins. The reflectivity profiles showed different evolutions according to the specific lipid mixtures and proteins, as shown in Fig. 3, where we report a summary of the reflectivity profiles in D_2O of the different SLB before and after the interaction with AFP and

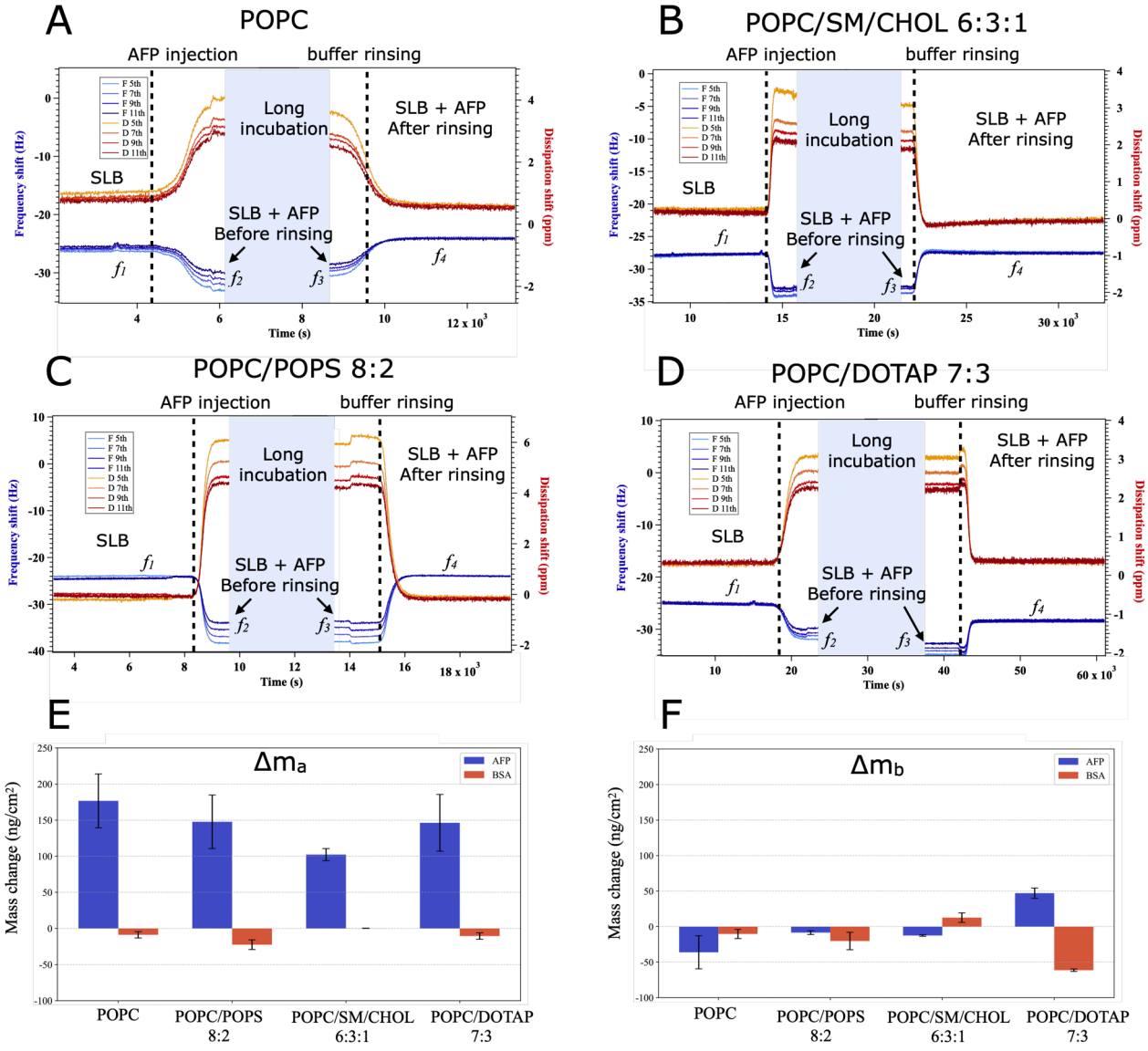

Fig. 2. Figures (A)-(D) represent different interaction behaviors for different SLBs in the presence of AFP after long incubation and rinsing with buffer. The graphs are an example of one measurement of each sample. (E) Histogram representing mass changes (Δm_a) at the sensor surface for different SLBs after the addition of AFP and BSA. (F) Histogram representing mass changes (Δm_b) at the sensor surface for different SLBs after the addition of AFP and BSA, long incubation, and rinsing with buffer. Error bars indicate the standard error, calculated from triplicate independent measurements.

BSA. In SLBs exposed to BSA, the effect on the reflectivity profile was minor, with the exception of the SLB made of POPC/POPS 8:2, where we observed significant differences between the reflectivity profiles before and after the exposure to the protein.

On the other hand, when the SLBs were exposed to AFP, we saw significant changes with all the SLBs, with the exception of the SLB made of POPC. The most drastic changes appeared in the case of POPC/POPS 8:2.

Among the tested models described in the Methods Section 2.4, only the best-fitting model for each sample is presented. The selection was based on the lowest normalised χ^2 value, complemented by the analysis of the Bayesian posterior distributions.

5.1. Interaction of SLBs with BSA

The analysis of BSA data, including model selection and Bayesian posterior evaluation, was performed in our previous work [30]. To summarize, BSA had negligible effects on the structure of POPC, POPC/SM/CHOL (6:3:1), and POPC/DOTAP (7:3) bilayers, as the reflectivity profiles remained unchanged after protein exposure. The only significant interaction was observed for POPC/POPS (8:2), where BSA penetration into the outer leaflet was detected, with a protein volume fraction of approximately 11% accompanied by increased hydration and interfacial roughness, consistent with partial lipid removal. A comparable effect was also reported previously for HSA interacting with PC/PS (8:2) bilayers [57]. These findings support the view that BSA interacts weakly with zwitterionic membranes but shows enhanced affinity for negatively charged bilayers, most likely mediated by localized cationic patches on the BSA surface [21,22,58].

5.2. Interaction of SLBs with AFP

5.2.1. POPC

Figure S8 (SI) shows the reflectivity profiles of the POPC SLB before and after exposure to AFP, along with the corresponding best-fit curves, scattering length density (SLD), and volume fraction profiles. After testing the different models (Table S1 in the supporting information), the model without the protein showing the smallest χ^2

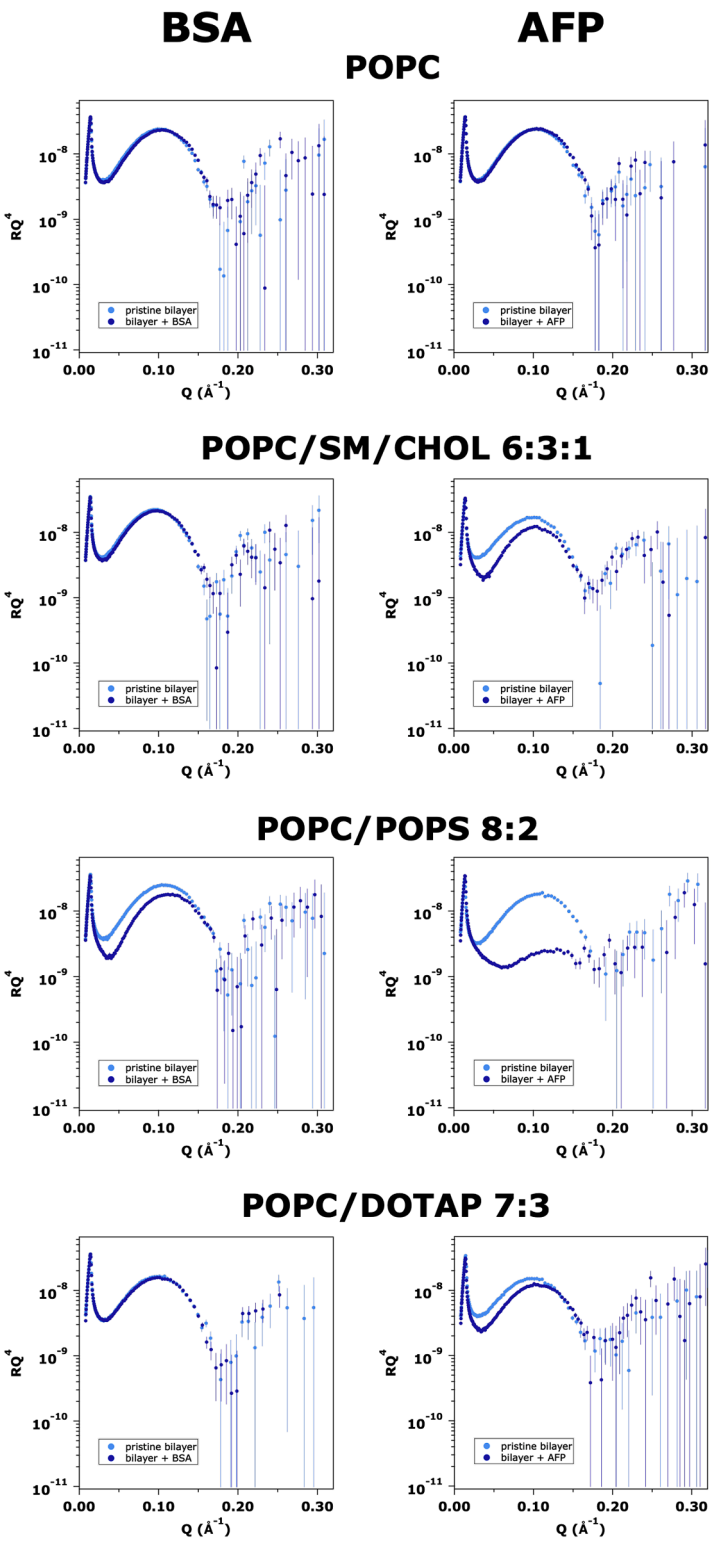

Fig. 3. Reflectivity profiles in the D_2O contrast for the four types of SLB before and after the exposure to BSA and AFP. BSA data from reference [30].

value was chosen as the one that best represented the data. Accordingly, the fitting parameters (Table 2) confirmed no relevant changes in the structural characteristics of the POPC bilayer upon AFP exposure. These results demonstrate that AFP does not significantly interact with or incorporate into POPC membranes under the conditions tested.

5.2.2. POPC/SM/Chol 6:3:1

Fig. 4 displays the reflectivity profiles at different contrasts of the SLB with composition POPC/SM/CHOL 6:3:1 before and after the exposure to AFP, together with the best-fit curves, SLD and volume fraction profiles. After testing different models and evaluating both χ^2 values and posterior distributions of key parameters, the best fit was obtained

with the partial incorporation of AFP into the outer leaflet without an additional adsorbed protein layer onto the SLB (model 3b, see Figure S1 in the SI). The χ^2 value obtained for Model 3, which includes a putative extra layer representing the portion of protein protruding into the aqueous phase above the bilayer, is very close to that of Model 3b. However, analysis of the posterior distributions for this model (corner plot in Figure S9 in the Supporting Information) indicated that the supplemental layer lacks physical relevance, as its thickness distribution peaks around 0 Å. Including such a layer would therefore count as overparameterization rather than providing a meaningful description of the system.

The selected model (fitting parameters shown in Table 2) indicates that AFP was incorporated in the outer leaflet of the SLB with a volume fraction of 38%. The incorporation of the protein is accompanied by a decrease in the thickness of the inner head region and an increase in the hydration of the SLB, especially in the proximal leaflet. The penetration of AFP into the outer leaflet might induce defects and disorder in the overall structure of the SLB, exposing the bilayer to penetration of water. In the distal leaflet, the water is replaced by the protein, mitigating the amount of water present in this region. In the proximal leaflet, the increase in the solvent penetration is likely linked to the removal of lipids after the interaction with the protein and successive rinsing of the liquid phase, which are not replaced by the proteins that remain in the distal region.

While the radius of gyration (Rg) of AFP has not been experimentally determined in literature, the protein shares a comparable molecular weight and overall fold with serum albumins. Accordingly, an Rg in the same range as that reported for albumins can be reasonably assumed as a first approximation. The radius of gyration for proteins such as human and bovine serum albumin is approximately 27–29 Å[18,59]. In low-resolution experiments like neutron reflectometry, this value represents the characteristic length scale associated with the protein's spatial distribution. Given that the thickness of the outer lipid leaflet is 23 Å and that this layer is typically smoothed by a 5 Å roughness on both interfaces, the effective thickness of the outer leaflet remains compatible with the incorporation of the protein within this region.

Based on these findings, AFP interacts with zwitterionic membranes containing SM and CHOL through partial incorporation into specific regions of the bilayer. This behavior might be likely influenced by the presence of ordered nanodomains, as the inclusion of SM and CHOL markedly alters AFP binding compared to pure POPC SLBs. These observations align with previous studies demonstrating the role of ordered nanodomains in promoting protein-lipid interactions [60–62].

5.2.3. POPC/POPS 8:2

As shown in Fig. 3, the interaction of AFP with the POPC/POPS (8:2) SLB induces drastic changes in the reflectivity profile. The reflectivity profiles of the SLB before and after the exposure to the AFP together with the fitting curves of the best model, and the resulting SLD and volume fraction profiles are reported in Figure S10. While the pristine SLB was well described using the standard bilayer model, none of the bilayer-based models could adequately fit the data after AFP exposure. A representative example of a fit using a model that includes a bilayer slab structure is presented in Figure S11 (Supporting Information). This figure highlights the significant discrepancies between the experimental reflectivity profiles and those generated by the model fit.

Instead, the simplest and more accurate representation of the data was obtained with a single unstructured slab of intermediate SLD between lipid and protein (model 6), indicating that the bilayer structure was heavily disrupted. These findings suggest that AFP strongly interacts with negatively charged membranes, where electrostatic interactions drive significant bilayer destabilization and mixing of lipids with proteins on the substrate.

5.2.4. POPC/DOTAP 70:30

The reflectivity profiles of the SLB with composition POPC/DOTAP 7:3 before and after the exposure to AFP together with the fitting curves of the best model and the resulting SLD and volume fraction profiles are reported in Figure S12 in the Supporting Information. In this case, the interaction with AFP was best represented by the formation of an adsorbed protein layer of approximately 39 Å thickness and a volume fraction of around 5%, without any incorporation of the protein into the SLB (model 1, see Figure S1). The fitting parameters are listed in Table 2. The resulting thickness of the adsorbed protein layer is consistent with physical dimensions of AFP. Moreover, the interaction with the proteins induces a thickening of the tail region and an increasing of hydration of the head and tail region. This is consistent with removal of a fraction of the lipids by AFP. Based on these results, electrostatic interactions between AFP and the positively charged lipid might be the main driving force for the observed behaviour, given that at physiological pH AFP is negatively charged.

Fig. 5 provides a summary of the NR results, highlighting the interactions of BSA and AFP with the four different lipid compositions.

6. Molecular dynamics simulations of protein-membrane interactions

6.1. Protein-membrane binding and contact frequency

To assess membrane association, we first computed the fraction of bound versus unbound states, defining a protein as "bound" when any of its non-hydrogen atoms were within 10 Å of a lipid (Fig. 6A). While both proteins display similar binding propensities, the extent and nature of their interactions depend strongly on the membrane composition. In particular, BSA and AFP remained closely associated with DOTAP-containing membranes throughout most of the simulation time, suggesting that electrostatic interactions are a key driver of membrane binding captured by the MD simulations. This trend was confirmed by a detailed contact analysis (Figure S13). Both proteins formed the highest number of contacts in DOTAP-containing membranes: BSA made ~ 74 lipid contacts, and AFP made ~ 100 contacts during the final 200 ns (Fig. 6B). For the other membrane compositions, contact numbers were lower and similar across both proteins. As all systems primarily contain POPC, it accounts for the majority of contacts; however, the presence of DOTAP enhances the interaction frequency.

6.2. Lipid occupancy and interaction surfaces

To further localize protein-lipid interaction sites, we analyzed lipid occupancies per residue over the final 200 ns of the simulation (Fig. 6C-E for AFP and S14A-C for BSA). Structural domains and subdomains of BSA and AFP were visualized based on previously established classifications (ref [63]. and ref [25]., respectively). Both proteins adopt heart-shaped, asymmetric folds dominated by α-helices and loop regions, and organized into three domains (I-III), each with two subdomains (A and B).

Fig. 6D (AFP) and S14B) (BSA) show lipid occupancies per residue for the four different membrane compositions: Lipid occupancies for both proteins are broadly distributed across all three domains, with domains I and II showing the highest values. In DOTAP-containing membranes, POPC exhibits the highest occupancy, consistent with the contact frequency analysis. For clarity, values above 40% were capped in the visualizations, although some residues reached up to 51% in BSA and 77% in AFP.

Finally, surface representations of lipid-interacting residues (Fig. 6E for AFP and S14C for BSA) revealed distinct interaction patterns. BSA showed a relatively uniform binding interface across domains I and II, whereas AFP's interactions were more localized, particularly around a flexible loop region that is absent in BSA. These findings suggest that specific structural motifs contribute to differences in membrane interaction between the two proteins.

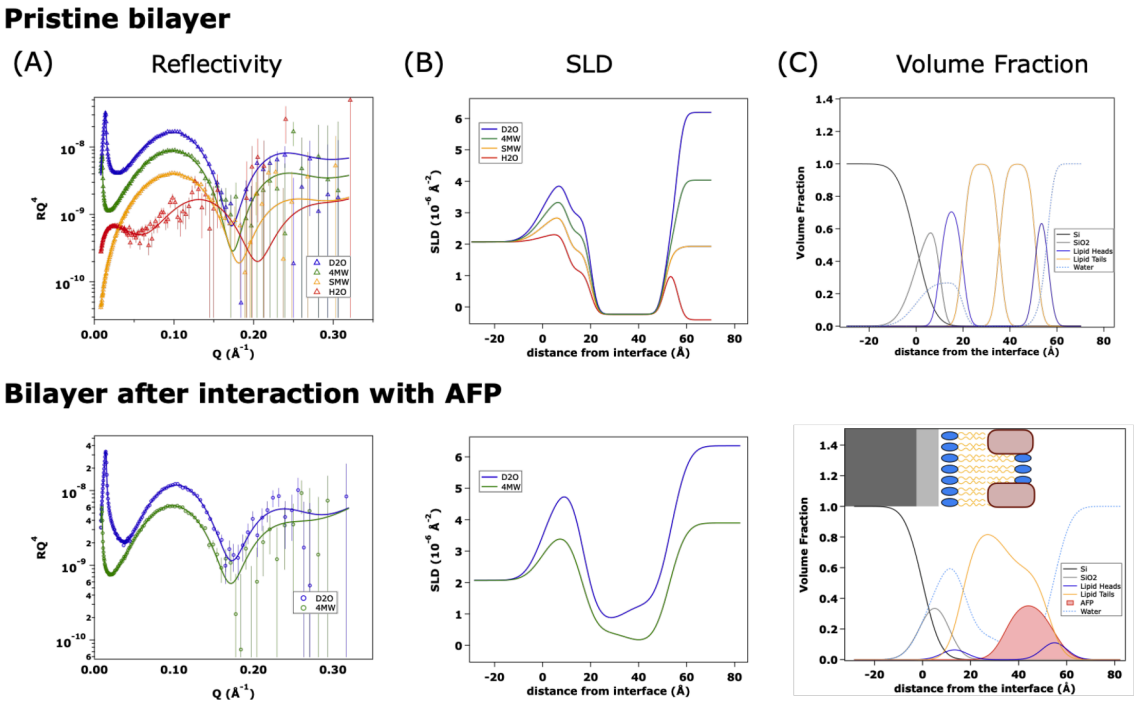

Fig. 4. Reflectivity curves and fits at different contrasts (A), the SLDs obtained from the analysis (B), and the corresponding volume fraction distribution (C) of the SLB POPC/SM/Chol 6:3:1 before and after the exposure to the AFP. Symbols represent the raw data; continuous lines represent the fit. The model that describes the experimental behavior better is the model representing a partial penetration of the protein in the outer leaflet of the lipid bilayer with no adsorbed layer of proteins onto the SLB (model 3b).

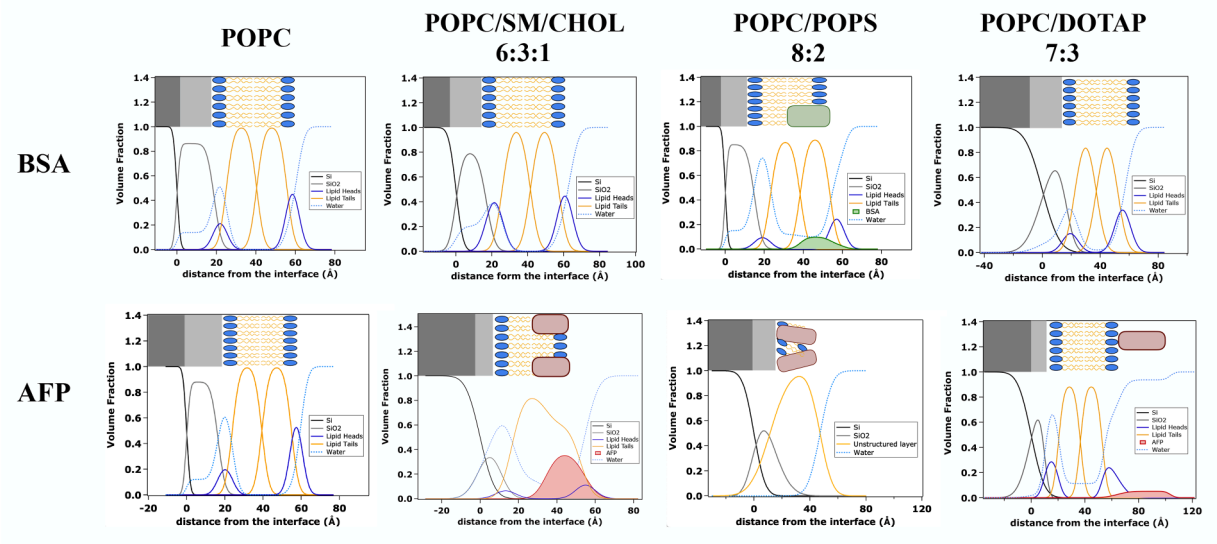

Fig. 5. Volume fraction profiles corresponding to the best-fit of the reflectivity data, illustrating how BSA and AFP interact with each of the four SLB lipid compositions. BSA data from reference [30].

6.3. Lipid depletion and enrichment near proteins

To investigate the local lipid composition around the proteins, we calculated the depletion/enrichment index (Fig. 7A), which compares the local abundance of lipids near the protein with its abundance in the bulk membrane. Surprisingly, POPS was the most enriched lipid near both proteins despite a relatively low overall contact number. In contrast, DOTAP was depleted in the vicinity of both BSA and AFP. This may seem counterintuitive given the large net negative charge of both proteins (BSA: -16e; AFP: -17e), but it reflects the presence of positively charged surface patches on the proteins that drive localized interactions (Figures S13 and S16 in the supporting information). This interpretation aligns with experimental findings that both proteins insert into POPS-containing supported bilayers. Cholesterol showed the most substantial depletion, likely due to its deep position within the membrane; almost no cholesterol molecules were detected within the 10 Åinteraction cut-off in any simulation snapshot.

6.4. Membrane thickness and domain formation

Next, we examined how lipid composition affects the membrane structure by calculating the average membrane thickness, defined as the

Table 2
Structural parameters of the SLBs before and after the exposure to the AFP. The corresponding fits are in Fig. 4, S8, S10, and S12. The values without error were fixed or kept at their nominal value.

Layer	Thickness [Å]	SLD [$\times 10^{-6}$ Å^{-2}]	Solvent [v/v]	Roughness [Å]
POPC				
SiO_2	16 ± 1	3.47	0.116 ± 0.003	2 ± 1
Inner headgroup	9 ± 1	1.88	0.58 ± 0.01	2 ± 1
Inner tail region	15 ± 1	-0.28	0.00 ± 0.01	2 ± 1
Outer tail region	15 ± 1	-0.28	0.00 ± 0.01	2 ± 1
Outer headgroup	5 ± 1	1.88	0.148± 0.009	2 ± 1
After exposure to AFP				
Inner headgroup	7 ± 1	1.88	0.751 ± 0.008	3 ± 1
Inner tail region	15 ± 1	-0.28	0.00 ± 0.01	3 ± 1
Outer tail region	15 ± 1	-0.28	0.00 ± 0.01	3 ± 1
Outer headgroup	5 ± 1	1.88	0.12 ± 0.01	3 ± 1
POPC/SM/CHOL 6:3:1				
SiO_2	10 ± 1	3.47	0.28 ± 0.01	6 ± 1
Inner headgroup	10 ± 1	1.725	0.27 ± 0.01	2 ± 1
Inner tail region	16 ± 1	-0.238	0.0011 ± 0.0002	2 ± 1
Outer tail region	16 ± 1	-0.238	0.0011 ± 0.0002	2 ± 1
Outer headgroup	5 ± 1	1.725	0.13 ± 0.04	2 ± 1
After exposure to AFP				
Inner headgroup	6 ± 1	1.725	0.87 ± 0.03	5 ± 1
Inner tail region	18 ± 1	-0.238	0.15 ± 0.02	5 ± 1
Outer tail region (*)	18 ± 1	-0.238	0.03 ± 0.02	5 ± 1
Outer headgroup (*)	5 ± 1	1.725	0.56 ± 0.4	5 ± 1
Volume fraction protein	0.38 ± 0.07	in the slabs labelled with *		
POPC/POPS 8:2				
SiO_2	11 ± 1	3.47	0.33 ± 0.003	6 ± 1
Inner headgroup	9 ± 1	2.285	0.20 ± 0.01	2 ± 1
Inner tail region	15 ± 1	-0.282	0.00 ± 0.01	2 ± 1
Outer tail region	15 ± 1	-0.282	0.00 ± 0.01	2 ± 1
Outer headgroup	5 ± 1	2.285	0.148 ± 0.009	2 ± 1
After exposure to AFP				
Unstructured layer	36 ± 1	2.49 ± 0.2	0.0003 ± 0.0001	11 ± 1
POPC/DOTAP 70:30				
SiO_2	10 ± 1	3.47	0.21 ± 0.01	8 ± 1
Inner headgroup	12 ± 1	1.796	0.31 ± 0.01	4 ± 1
Inner tail region	14 ± 1	-0.262	0.002 ± 0.003	4 ± 1
Outer tail region	14 ± 1	-0.262	0.002 ± 0.003	4 ± 1
Outer headgroup	6 ± 1	1.796	0.17 ± 0.01	4 ± 1
After exposure to AFP				
Inner headgroup	11 ± 1	1.796	0.68 ± 0.07	3 ± 1
Inner tail region	16 ± 1	-0.262	0.109 ± 0.004	3 ± 1
Outer tail region	16 ± 1	-0.262	0.109 ± 0.004	3 ± 1
Outer headgroup	11 ± 1	1.796	0.67 ± 0.05	3 ± 1
Protein layer (*)	39 ± 1		0.948 ± 0.005	8 ± 1
Volume fraction protein	0.052 ± 0.005	in the slabs labelled with *		

distance between phosphate groups in opposing leaflets (Fig. 7B). The pure POPC bilayer showed a thickness of 39.0 ± 0.3 Å. Adding charged lipids (POPS, DOTAP) caused a slight thickening, whereas the inclusion of NSM and cholesterol had a more pronounced effect, increasing the thickness by ~ 4.5 Å. The spatially resolved thickness maps (Fig. 7D) revealed that most membranes were laterally homogeneous, except the NSM/CHOL-containing system. In this case, local deviations exceeding 3 Å from the mean (43.5 ± 0.3 Å) suggest the formation of nanodomains. To explore these potential nanodomains further, we quantified the local lipid environment using neighborhood enrichment analysis (Fig. 7D; see Methods). This analysis characterizes the composition of lipid patches surrounding each reference lipid. Heat maps of depletion/enrichment values, averaged over 10 independent replicas from 300 ns onward, show that the local environment around POPC is consistently depleted. At the same time, the area surrounding NSM lipids is strongly enriched, indicating localized lipid clustering. In particular, cholesterol (CHOL) is markedly enriched near NSM, supporting the presence of NSM/CHOL-rich domains and POPC-rich regions with a lower packing density.

These lateral patterns were further confirmed by normalizing lipid densities to a uniform distribution, yielding the 2D depletion/enrichment maps shown in Figure S15 A-B for CHOL and NSM in the upper leaflet. Strong enrichment of CHOL near NSM-rich patches was again observed and is visually confirmed in the simulation snapshot shown in Figure S15C.

7. Discussion

To investigate the interaction mechanisms of BSA and AFP with supported lipid bilayers (SLBs) of varying compositions, we employed two complementary experimental techniques, QCM-D and NR, in combination with MD simulations. This integrated approach allowed us to capture both nanoscopic binding behavior and molecular-level structural details.

The integration of QCM-D data with NR results provided valuable insights into how the interaction of the biomarker AFP with SLBs is influenced by the lipid composition of the bilayer. QCM-D and NR probe the protein-lipid bilayer system with fundamentally different sensitiv-

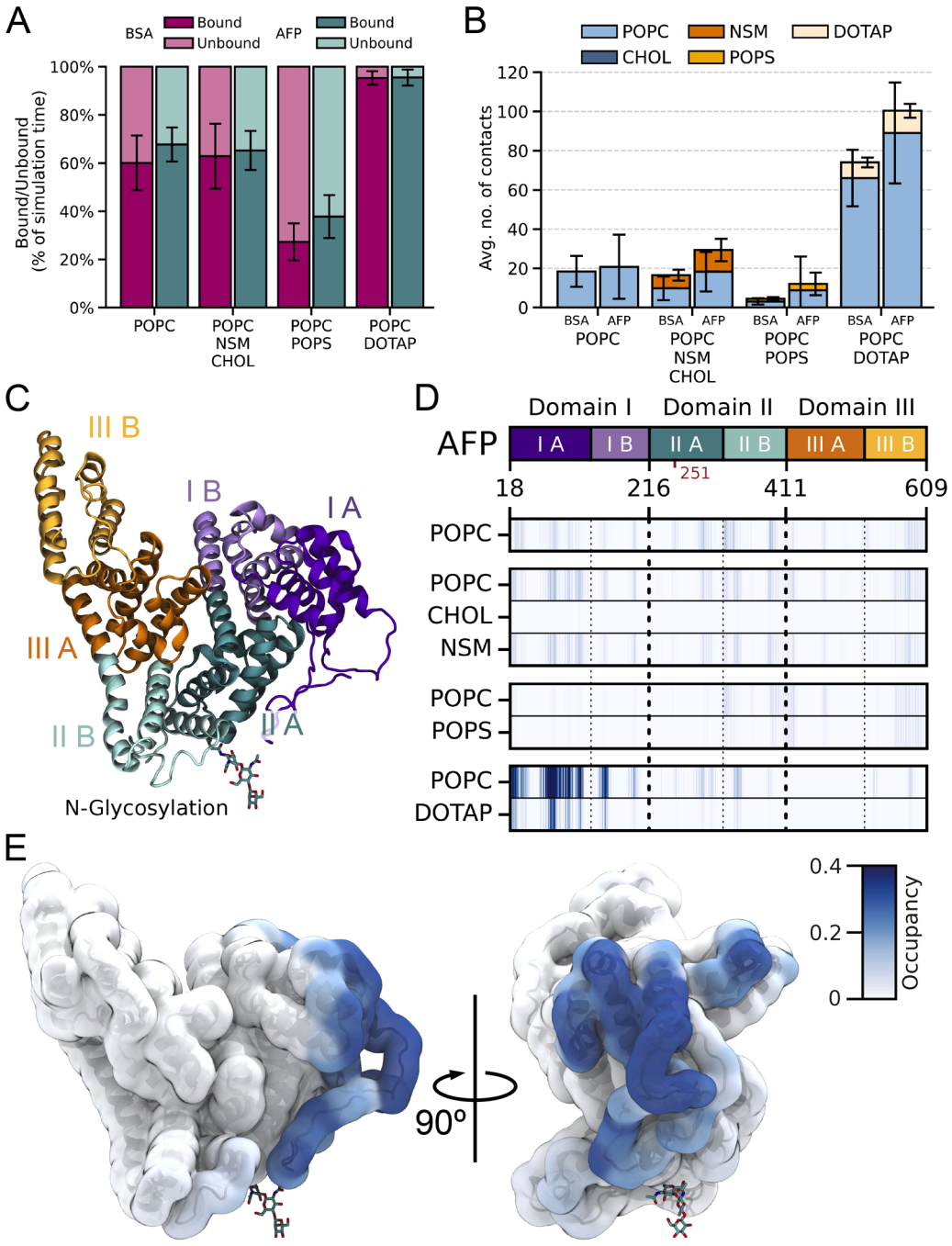

Fig. 6. MD simulations of BSA and AFP interacting with four different membranes (pure POPC; POPC/POPS 8:2; POPC/DOTAP 7:3; and POPC/NSM/CHOL 6:3:1. (A) Bound vs. unbound states and (B) protein-lipid contacts per lipid type are averaged over 10 replicas; error bars indicate standard deviation. (C) Protein structure of AFP with color-coded domains (I-III) and subdomains (A and B) and N-glycosylation at N251. (D) Occupancy per AFP residue for each lipid type. Protein domains and subdomains are indicated using the same color code in (C). (E) Surface representation of AFP highlights the regions of highest lipid occupancies with DOTAP-containing membranes.

ities. QCM-D provides an accurate measurement of the total coupled mass (including hydrodynamically coupled water) associated with the surface, but it cannot unambiguously distinguish whether a mass change originates from lipids, proteins, or changes in hydration. NR, on the other hand, is intrinsically sensitive to the individual scattering length densities (SLDs) of lipids, proteins, and water. This allows a more direct structural and compositional analysis of the bilayer. Furthermore, performing NR at multiple D_2O/H_2O contrasts enables the disentanglement of solvent contributions from the organic components, thereby allowing us to resolve protein incorporation even in cases where lipid depletion occurs. Taken together, these two techniques provide complementary information: QCM-D captures global mass and viscoelastic changes associated with adsorption and lipid rearrangement, while NR reveals the molecular distribution of proteins and lipids within the bilayer, including changes in overall bilayer thickness, in the thickness of individual sub-layers, and in their hydration, roughness, and leaflet composition in response to protein binding. MD simulations were employed to provide an atomic-scale perspective on the interactions between in silico-generated lipid bilayers and proteins. These simulations offered complementary insight into how lipid composition, bilayer organiza-

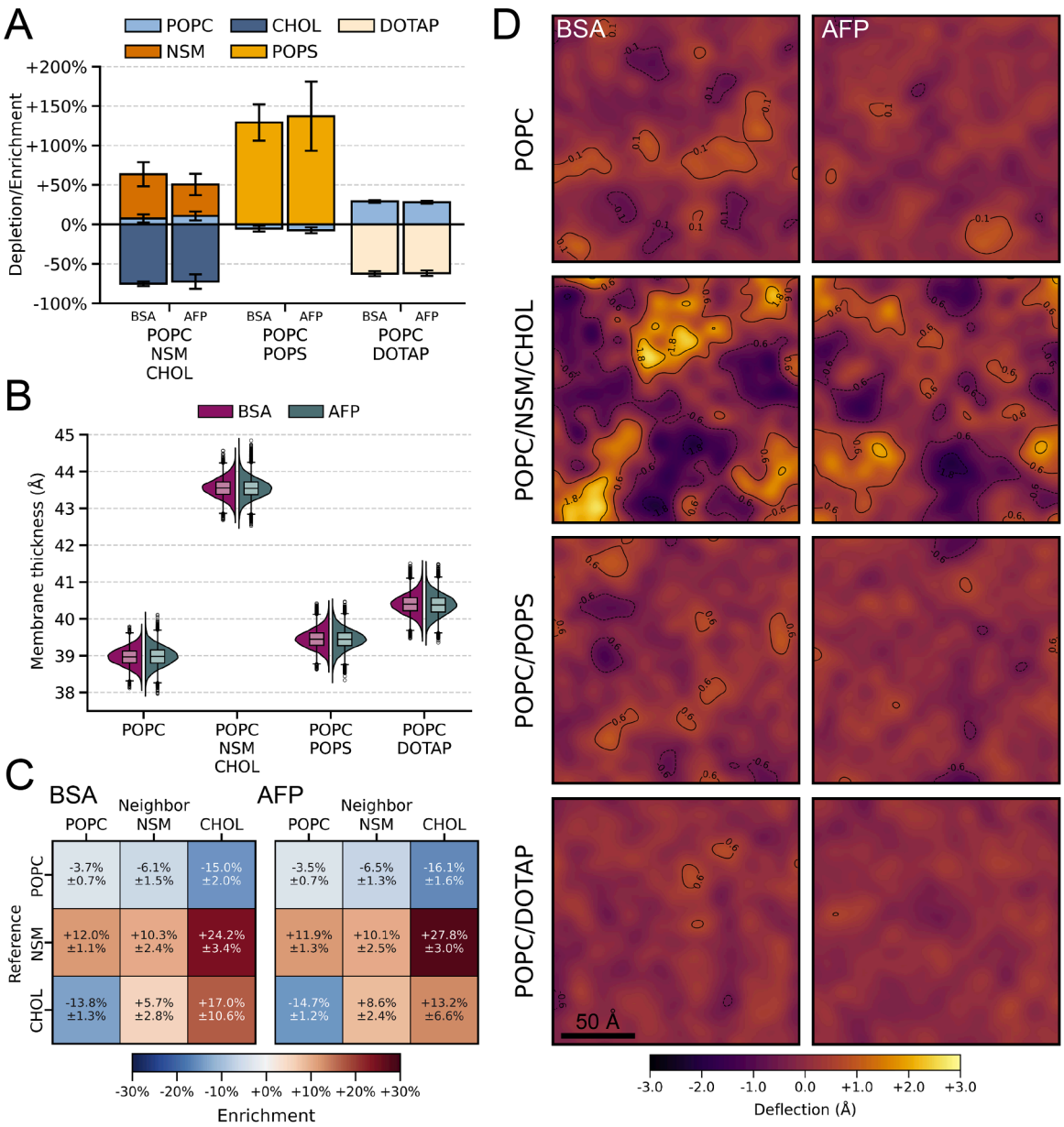

Fig. 7. (A) Depletion/enrichment of lipids within 10 Åcutoff of BSA and AFP in membrane-bound states averaged over 10 replicas; error bars indicate standard deviation. (B) Box plot/violin plot of the membrane thickness for the four different membrane compositions in the presence of BSA and AFP. The data combines each simulation frame from all 10 replicas starting at 300 ns (n = 20,000 per membrane composition). (C) Heat maps of lipid neighborhood enrichment averaged over 10 replicas; error bars indicate standard deviation. (D) 2D deflection of membrane thickness with respect to the average thickness of a single replica for the four different membrane compositions in the presence of BSA and AFP averaged over the last 200 ns.

tion, and protein surface characteristics govern protein-lipid interactions.

While direct comparison with in vitro experiments cannot be expected due to intrinsic methodological differences, MD nonetheless yields mechanistic details that help interpret experimental findings. The main differences between the approaches arise from the distinct timescales and system configurations they probe. Reflectometry and QCM-D capture near-equilibrium structures over minutes to hours, whereas MD explores dynamics on nanosecond-microsecond timescales. Moreover, the simulated bilayer is free-standing, laterally finite, and idealized-lacking the substrate effects or imperfections present in the SLBs used experimentally. In vitro systems extend over much larger surface area, increasing the likelihood of structural defects such as domain boundaries, pinholes, or discontinuities, which may influence protein-bilayer interactions. Finally, the simulations model a single protein interacting with the membrane and therefore do not account for potential cooperative effects such as clustering, crowding, or cooperative insertion, which could significantly influence the nature and extent of protein-bilayer interactions [64]. These effects, however, were beyond the scope of the present MD simulations but remain an important avenue for future investigation.

As shown in Fig. 6 A-D, which provides a visual summary of the interactions between the two proteins and the various lipid bilayers, the bound/unbound fractions (panel A), as well as the average number of contacts and contact occupancy (panels B and D), are highest for the POPC/DOTAP bilayer. However, this elevated level of interaction does not correspond to the strongest effect observed in the neutron scattering experiments, which instead identified POPC/POPS as the bilayer composition with the most pronounced structural changes. Interestingly, the MD simulations showed that POPC/POPS exhibited the lowest average

number of contacts, emphasizing that MD simulations alone may not fully capture the complexity of experimentally observed behaviors, as previously noted. Nevertheless, when comparing the relative interaction profiles of AFP and BSA across all lipid compositions, the experimentally observed trend of generally stronger AFP-bilayer interactions is consistently reflected in the simulation results. These contrasting interaction patterns provide valuable insights into the distinct ways each protein engages with the lipid bilayers.

To integrate the experimental and computational findings, we discuss the interactions of BSA and AFP with each lipid composition sequentially, combining QCM-D, NR, and MD results for a comprehensive picture.

7.1. Membrane composed of POPC

For the pure zwitterionic POPC SLB, both experimental techniques indicated negligible interaction with AFP or BSA. QCM-D showed either a slight net negative mass balance upon AFP exposure or only minor variations within experimental error for BSA, while NR confirmed the absence of structural perturbations, with the best-fitting model corresponding to no interaction. These results are consistent with MD simulations, which showed that although both proteins contacted the bilayer in approximately 60% of the frames (Fig. 6A), the average number of contacts and contact occupancy remained very low (Fig. 6B, D), indicative of non-specific binding, with no particular region of the proteins engaging strongly with the membrane. The overall contact levels were comparable between AFP and BSA.

7.2. Membrane composed of POPC/CHOL/SM

With the mixed zwitterionic lipid composition, POPC/SM/CHOL SLB, AFP exhibited a significant interaction, in contrast to its negligible effect on pure POPC. QCM-D measurements indicated a net decrease in the total adsorbed mass after exposure to AFP and subsequent buffer rinsing. In contrast, NR data were best described by a model incorporating AFP within the outer leaflet of the SLB, with a volume fraction of 38%, accompanied by a 15% increase in lipid hydration, suggesting partial lipid removal. This apparent discrepancy can be explained by considering the simultaneous interplay of lipid desorption and protein incorporation, leading to a complex structural rearrangement at the interface. The net negative mass detected by QCM-D points toward a dominant lipid loss, whereas NR emphasizes the concurrent protein insertion and increased bilayer hydration. While the NR model supports the presence of incorporated protein, it does not allow definitive quantification of lipid loss, leaving some uncertainty in the net mass balance. Overall, given that the interaction of AFP with pure POPC bilayer was undetectable by both NR and QCM-D, these findings suggest that ordered lipid domains, stabilized by SM and CHOL, may play a critical role in modulating AFP interaction. In contrast, BSA showed no measurable interaction in either technique.

In the presence of SM and CHOL, MD simulations reveal an increase in bilayer thickness (~ 4 Å) compared to all other systems studied (Fig. 7B), in agreement with NR and QCM-D results. Interestingly, despite the low number of protein-lipid contacts, simulations show a ~ 50% enrichment of SM near the proteins (Fig. 7A), suggesting a preference for sphingomyelin-rich domains over pure POPC regions. CHOL, on the other hand, is strongly depleted near the adsorbed proteins because it resides deeper within the membrane, beyond the immediate protein-lipid interface. However, CHOL exhibits a strong tendency to colocalize with SM, highlighting their mutual affinity, as shown in the lipid neighborhood enrichment heatmaps (Fig. 7C). This co-localization is further supported by the two-dimensional enrichment maps of CHOL and SM of the POPC/SM/CHOL membranes in the presence of BSA and AFP (Figure S15(A-C). Together, these findings suggest the formation of cholesterol- and sphingomyelin-enriched nanodomains characterized by significant local thickness variations, as shown in Fig. 7D.

Although the simulations do not fully align with experimental results, which show that only AFP significantly interacts with the bilayer, they may help explain the observed differences compared to the POPC pure system. Specifically, the formation of localized sphingomyelin-cholesterol-enriched patches appears to influence protein-membrane interactions and may be the basis for the distinct behavior of AFP and BSA in this ternary bilayer system, as the flexible loop region present in the AFP - and absent in the BSA - contributes to bindings by forming more contacts, suggesting that binding events might be more stable with AFP.

7.3. Membrane composed by POPC/POPS

For the anionic bilayer containing POPS, both QCM-D and NR consistently indicated strong protein-membrane interactions, though with different outcomes for AFP and BSA. AFP induced substantial lipid removal, leading to large-scale bilayer disruption. The effect was significantly more pronounced in the NR data, which allowed for a detailed assessment of the substantial structural impact of AFP on the bilayer. NR revealed that AFP transformed the bilayer into an unstructured layer of mixed proteins and lipids, while QCM-D showed a net negative total adsorbed mass following protein exposure and rinsing with buffer, consistent with the predominant lipid loss. Although NR could not resolve the precise structural details related to the loss of material, the overall thinning of the bilayer is in agreement with the results from QCM-D. For BSA, the combined analysis was consistent with lipid removal accompanied by the adsorption and/or incorporation of BSA into the SLB. QCM-D detected a net decrease in total adsorbed mass, reflecting a greater loss of lipids relative to protein incorporation. NR provided further insight, with the best-fitting model indicating 11% protein incorporation and a significant increase in solvent content within the bilayer, corresponding to 22% hydration of the tail region. Together, these findings demonstrate that both proteins perturb the negatively charged bilayer, but AFP induces a more drastic structural rearrangement compared to BSA.

However, POPC/POPS SLB showed the greatest discrepancy between simulations and experimental results, particularly in terms of absolute interaction strength. Whereas experiments revealed the strongest perturbations for both proteins, simulations showed the lowest overall number of protein-lipid contacts (Fig. 6A-B). However, when considering the relative interaction strength between the two proteins, the simulations still captured the experimental trend: AFP exhibited a stronger interaction with the bilayer than BSA, based on the number of contacts. Clearly, additional factors must be considered when evaluating how these proteins interact with anionic lipid bilayers. From the simulation perspective, the low number of interactions may stem from the high net negative charges of the proteins (BSA: -16e; AFP: -17e), which could generate electrostatic repulsion with the negatively charged bilayer and hinder membrane association within the simulation timescale. This suggests that protein adsorption may be kinetically limited due to energy barriers.

Surprisingly, as shown by the enrichment data in Fig. 7A, both proteins exhibit the highest level of PS lipid enrichment in their vicinity (exceeding 100%). This is likely due to positively charged surface patches, sparsely distributed on the proteins, as illustrated in Figure S16. Despite the lack of direct agreement with experimental data, potentially due to kinetic barriers and concentration-dependent effects, simulations suggest that once proteins approach the membrane surface, they tend to cluster PS lipids.

7.4. Membrane composed of POPC/DOTAP

For the cationic bilayer containing DOTAP, both experimental techniques revealed the formation of an AFP protein layer adsorbed on top of the SLB, with minimal impact on the bilayer's structure. This conclusion was supported by QCM-D data, which showed a net increase in total adsorbed mass after rinsing with buffer, and corroborated by NR

results, where the best-fitting model indicated the presence of an adsorbed protein layer approximately 39 Å thick. This thickness value is approximately 25% greater than the radius of gyration associated with albumins, such as those used in this study. Such a discrepancy suggests a preferential orientation of the adsorbed AFP relative to the lipid bilayer. If AFP adopts an orientation where one of its dimensions is significantly larger than the others, this could directly impact the measured thickness of the adsorbed protein layer. As illustrated in Fig. 6E, DOTAP preferentially interacts with the flexible domain I of AFP, which may further influence the protein's orientation and the resulting layer thickness. These observations indicated that electrostatic forces may play a primary role in modulating the interaction between the net negatively charged AFP (at physiological pH) and the positively charged lipid, DOTAP. In the case of BSA, QCM-D measurements revealed a significant lipid removal from the bilayer, as indicated by a net decrease in total adsorbed mass following protein exposure. Conversely, NR did not detect any appreciable adsorption or incorporation of the protein within the SLB structure.

For this lipid composition, MD simulations revealed the strongest protein-lipid interactions, measured by the number of contacts, among all lipid compositions examined (Fig. 6). Notably, AFP establishes more contacts with the membrane than BSA, suggesting a higher membrane affinity. For AFP, lipid contacts are predominantly localized around domain 1A (Figs. 6D and E), indicating a well-defined interaction interface. A close-up view in Figure S13B reveals that a specific region of the protein (residues 69–100) is primarily responsible for engaging with the membrane. This could explain the membrane adsorption observed experimentally. In contrast, BSA's lipid interactions, though comparable in contact number, are more broadly distributed across domains I and II and involve distinct negatively charged residues (Figures S14C and S13A). This suggests the presence of two distinct binding motifs in BSA, which, although capable of supporting interactions in MD simulations (driven by electrostatic forces and limited sampling), may not be sufficient to promote stable membrane association under experimental conditions.

Interestingly, across all simulations, no significant interactions were observed between the membrane and the glycosylated moiety near residue N251 of AFP. This suggests that the glycosylation site does not play a major role in membrane binding under the tested conditions. Instead, structural features such as domain flexibility seem to have a greater influence on protein-membrane interactions.

8. Conclusions

Our study elucidates the interactions of the clinical biomarker alphafetoprotein, as well as bovine serum albumin, with model lipid membranes, offering novel insights relevant to both fundamental biophysics and biomarker detection applications. To our knowledge, this is the first report on the interaction of AFP with supported lipid bilayers. Our findings demonstrate that AFP engages significantly with lipid moieties, with the strength and nature of this interaction being highly dependent on the lipid composition of the membrane. Across all lipid compositions, the electrostatic interaction of the membrane surface emerges as a dominant factor modulating protein-membrane binding, alongside lipid packing and phase behavior. However, the contrasting behaviours of AFP and BSA observed experimentally demonstrate that these effects depend not only on membrane composition but also on the proteins' structural features and contact geometry. Although both proteins exhibit a similarly asymmetric charge distribution (see electrostatic potential map in Supplementary Figure S15), with negatively charged residues predominantly solvent-exposed and positively charged residues largely buried, their interaction interfaces differ markedly. In AFP, membrane interaction is dominated by domain IA, where a flexible loop region enables the protein to present a larger, contiguous contact area to the membrane (Figure Fig. 6E). Although AFP contains a single N-glycan located near the membrane-interaction interface and adjacent to the flexible loop in domain IA, our simulations do not reveal any substantial glycan-lipid interactions, indicating that glycosylation plays a minimal direct role in the present simulations. In contrast, BSA forms interactions through multiple, spatially separated motifs located mainly in domains IA and IIB, thereby preventing simultaneous formation of these contacts (Supplementary Figure S13D). This structural distinction could indicate the more substantial and more disruptive interactions observed for AFP across several lipid systems in experiments. This difference is particularly evident in systems containing positively charged lipids, which strongly promote the association of AFP and BSA with the bilayer in the simulations. In the cationic POPC/DOTAP bilayer, AFP displays strong, experimentally supported adsorption with minimal structural perturbation, consistent with MD simulations that reveal the highest protein-lipid contact density across all lipid compositions and a well-defined interaction interface primarily involving domain IA. BSA, by contrast, does not form an equivalently stable adsorbed layer in NR experiments, reflecting the fact that its membrane contacts might be split, as suggested by MD simulations, between IA and IIB and therefore cannot contribute cooperatively to binding. Conversely, the anionic POPC/POPS bilayer shows the most severe structural disruption, with NR indicating extensive lipid removal and bilayer collapse. Although MD simulations report the lowest overall contact number for this lipid composition, they reveal the highest local enrichment of POPS lipids around the proteins, suggesting that proteins preferentially recruit anionic lipids despite limited contact persistence. This behaviour is similar to the mechanism described by Lolicato et al. [64], in which cationic nanoparticles extract lipids by recruiting negatively charged lipids to their surface. While AFP is not globally cationic, the geometry of its IA domain interface allows the simultaneous formation of several short-lived contacts, which, over longer timescales, may support POPS recruitment and thus contribute to the experimentally observed membrane destabilization. BSA, by contrast, interacts with POPS less efficiently, consistent with its separated interacting motifs and reduced ability to form multiple concurrent contacts, possibly explaining its partial insertion and moderate thinning rather than complete bilayer collapse. In the mixed zwitterionic POPC/SM/CHOL system, lipid packing and phase organization are central to understanding different protein behaviors observed in experiments. Although AFP and BSA do not show markedly different membrane-contact levels in the simulations, the membrane features captured computationally, i.e., SM/CHOL-enriched nanodomains and local bilayer thickening, provide a coherent framework for interpreting the experimental differences. These structural heterogeneities offer a mechanistic basis for the partial protein incorporation and increased hydration detected by NR. Finally, in pure POPC, where charge effects and ordered domains are lacking, both techniques agree that the interaction is negligible for both proteins. Together, these results indicate that the experimentally observed compositional dependencies arise from a balance of electrostatics, local packing density, domain-specific phase behavior, as well as differences in structural flexibility and in the simultaneous contact-formation capability that distinguish AFP from BSA.

These observations have important implications for conventional tumor assays, such as ELISA, where such lipid-protein interactions may influence assay performance and interpretation.

Notably, in our previous work on glycated BSA (gBSA) [30], we demonstrated that glycation enhances the interaction of BSA with negatively charged membranes. This finding suggests that carbohydrate-related modifications can modulate protein-membrane interactions by altering both surface charge and protein conformation. By analogy, investigating how the removal of N-linked glycans influences AFP-membrane binding would be highly informative. Future studies comparing native and deglycosylated AFP on SLBs, particularly those composed of POPC/POPS, could elucidate the specific role of glycosylation in these interactions. Furthermore, extending this approach to biomarkers with higher glycosylation levels, such as soluble vascular endothelial cadherin [65,66], would provide valuable additional insights.

Overall, our study provides new insights into how clinically relevant proteins, such as AFP and BSA, interact with model lipid membranes. These findings could contribute to a better understanding of protein-membrane interactions and may offer considerations for future biomarker detection strategies.

CRediT authorship contribution statement

Beatrice Barletti: Writing – review & editing, Writing – original draft, Investigation, Formal analysis, Data curation, Conceptualization; **Melanie König:** Writing – review & editing, Writing – original draft, Software, Formal analysis, Data curation; **Nicoló Paracini:** Writing – review & editing, Validation, Supervision, Investigation, Data curation, Conceptualization; **Giovanna Fragneto:** Writing – review & editing, Supervision, Data curation, Conceptualization; **Jean-Pierre Alcaraz:** Writing – review & editing, Validation, Conceptualization; **Andrew Nelson:** Writing – review & editing, Software; **Isabelle Vilgrain:** Writing – review & editing, Validation, Conceptualization; **Donald K. Martin:** Writing – review & editing, Writing – original draft, Supervision, Funding acquisition, Conceptualization; **Fabio Lolicato:** Writing – review & editing, Writing – original draft, Supervision, Methodology, Formal analysis, Data curation, Conceptualization; **Marco Maccarini:** Writing – review & editing, Writing – original draft, Validation, Supervision, Methodology, Investigation, Funding acquisition, Formal analysis, Data curation, Conceptualization.

Data availability

Data will be made available on request.

Declaration of competing interest

The authors declare that they have no known competing financial interests or personal relationships that could have appeared to influence the work reported in this paper.

Acknowledgements

We acknowledge the InnovaXN (European Union's Horizon 2020 research and innovation programme under the Marie SkÅĆodowska-Curie grant agreement no. 847439) for funding the InnovaXN-25-2020 project, the Institut Laue-Langevin, which provided allocation of neutron beam time (Experiment DOI: doi-10.5291/ILL-DATA.9-13-1048, doi-10.5291/ILL-DATA.9-13-1084, doi-10.5291/ILL-DATA.9-13-1125), and the use of Partnership for Soft Condensed Matter laboratories. This work is supported by grants of the Deutsche Forschungsgemeinschaft to FL (SFB-1638/1 - 511488495 - Z01). FL acknowledged the computing resources provided by the CSC - IT Center for Science Ltd. (Espoo, Finland) and supported by the state of Baden-Württemberg through bwHPC and the German Research Foundation (DFG) through grant INST 35/1597-1 FUGG. FL and MK gratefully acknowledge the data storage service SDS@hd supported by the Ministry of Science, Research and the Arts Baden-Württemberg (MWK) and the German Research Foundation (DFG) through grant INST 35/1503-1 FUGG.

Supplementary material

Supplementary material associated with this article can be found in the online version at 10.1016/j.jcis.2025.139753

References

[1] Y. Tanaka, H. Akiyama, T. Kuroda, G. Jung, K. Tanahashi, H. Sugaya, J. Utsumi, H. Kawasaki, H. Hirano, A novel approach and protocol for discovering extremely low-abundance proteins in serum, Proteomics 6 (2006) 4845–4855. https://doi.org/10.1002/pmic.200500774

[2] K.R. Feingold, B. Anawalt, M.R. Blackman, et al., Introduction to lipids and lipoproteins, eds. Endotext. South Dartmouth (MA) (2024).

[3] A. Khalil-Mgharbel, H. Polena, P.K. Dembélé, M.M. Hasan Sohag, J.-P. Alcaraz, D.K. Martin, I. Vilgrain, A biomimetic lipid membrane device reveals the interaction of cancer biomarkers with human serum lipidic moieties, Biotechnol. J. 13 (12) (2018) 1800463.

[4] D. Calvo, D. Gómez-Coronado, M.A. Lasunción, M.A. Vega, CLA-1 is an 85-kD plasma membrane glycoprotein that acts as a high-affinity receptor for both native (HDL, LDL, and VLDL) and modified (OxLDL and AcLDL) lipoproteins, Arterioscler. Thromb. Vasc. Biol. 17 (11) (1997) 2341–2349.

[5] Y.M. Park, CD36, A scavenger receptor implicated in atherosclerosis, Exper. Molecular Med. 46 (6) (2014) e99–e99.

[6] A. Rigotti, S.L. Acton, M. Krieger, The class B scavenger receptors SR-BI and CD36 are receptors for anionic phospholipids, J. Biol. Chem. 270 (27) (1995) 16221–16224.

[7] L. Cocquerel, C. Voisset, J. Dubuisson, Hepatitis C virus entry: potential receptors and their biological functions, J. Gen. Virol. 87 (5) (2006) 1075–1084.

[8] B. Bartosch, G. Verney, M. Dreux, P. Donot, Y. Morice, F. Penin, J.-M. Pawlotsky, D. Lavillette, F.-L. Cosset, An interplay between hypervariable region 1 of the hepatitis C virus E2 glycoprotein, the scavenger receptor BI, and high-density lipoprotein promotes both enhancement of infection and protection against neutralizing antibodies, J. Virol. 79 (2005) 8217–8229. https://doi.org/10.1128/jvi.79.13.8217-8229.2005

[9] B.A. Cornell, V.L.B. Braach-Maksvytis, L.G. King, P.D.J. Osman, B. Raguse, L. Wieczorek, R.J. Pace, A biosensor that uses ion-channel switches, Nature 387 (1997) 580–583. https://doi.org/10.1038/42432

[10] B.A. Cornell, G. Krishna, P.D. Osman, R.D. Pace, L. Wieczorek, Tethered-bilayer lipid membranes as a support for membrane-active peptides, Biochem. Soc. Trans. 29 (2001) 613–617. https://doi.org/10.1042/BST0290613

[11] K.D. Martin, Nanobiotechnology of Biomimetic Membrane, Springer, New York, New York, 2007.

[12] E. Ruoslahti, M. Seppälä, Studies of carcino-fetal proteins: physical and chemical properties of human α-fetoprotein, Int. J. Cancer 7 (2) (1971) 218–225.

[13] C.-W. Lee, H.-I. Tsai, W.-C. Lee, S.-W. Huang, C.-Y. Lin, Y.-C. Hsieh, T. Kuo, C.-W. Chen, M.-C. Yu, Normal alpha-fetoprotein hepatocellular carcinoma: are they really normal?, J. Clin. Med. 8 (10) (2019) 1736.

[14] R. Masuzaki, S.J. Karp, M. Omata, New serum markers of hepatocellular carcinoma, Semin. Oncol. 39 (4) (2012) 434–439.

[15] A.X. Zhu, Y.-K. Kang, C.-J. Yen, R.S. Finn, P.R. Galle, J.M. Llovet, E. Assenat, G. Brandi, M. Pracht, H.Y. Lim, et al., Ramucirumab after sorafenib in patients with advanced hepatocellular carcinoma and increased α-fetoprotein concentrations (REACH-2): a randomised, double-blind, placebo-controlled, phase 3 trial, The Lancet Oncology 20 (2) (2019) 282–296.

[16] F. Piñero, M. Dirchwolf, M.G. Pessôa, Biomarkers in hepatocellular carcinoma: diagnosis, prognosis and treatment response assessment, Cells 9 (6) (2020) 1370.

[17] E. Waidely, A.-R.O. Al-Yuobi, A.S. Bashammakh, M.S. El-Shahawi, R.M. Leblanc, Serum protein biomarkers relevant to hepatocellular carcinoma and their detection, Analyst 141 (1) (2016) 36–44.

[18] D.-M. Smilgies, E. Folta-Stogniew, Molecular weight–gyration radius relation of globular proteins: a comparison of light scattering, small-angle X-ray scattering and structure-based data, Appl. Crystallogr. 48 (5) (2015) 1604–1606.

[19] K. Garapati, A. Jain, B.J. Madden, D.-G. Mun, J. Sharma, R. Budhraja, A. Pandey, Defining albumin as a glycoprotein with multiple N-linked glycosylation sites, J. Transl. Med. 22 (1) (2024) 454.

[20] C.-Y. Shen, C.-H. Wu, C.-H. Lu, Y.-M. Kuo, K.-J. Li, S.-C. Hsieh, C.-L. Yu, Advanced glycation end products of bovine serum albumin suppressed Th1/Th2 cytokine but enhanced monocyte IL-6 gene expression via MAPK-ERK and MyD88 transduced NF-κB p50 signaling pathways, Molecules 24 (13) (2019) 2461.

[21] I.R. Krauss, A. Picariello, G. Vitiello, A. De Santis, A. Koutsioubas, J.E. Houston, G. Fragneto, L. Paduano, Interaction with human serum proteins reveals biocompatibility of phosphocholine-Functionalized SPIONs and formation of albumin-decorated nanoparticles, Langmuir 36 (2020) 8777–8791. https://doi.org/10.1021/acs.langmuir.0c01083

[22] F. Ruggeri, F. Zhang, T. Lind, E.D. Bruce, B.L.T. Lau, M. Cárdenas, Non-specific interactions between soluble proteins and lipids induce irreversible changes in the properties of lipid bilayers, Soft Matter 9 (2013) 4219–4226. https://doi.org/10.1039/c3sm27769k

[23] D.M. Charbonneau, H.A. Tajmir-Riahi, Study on the interaction of cationic lipids with bovine serum albumin, J. Phys. Chem. B 114 (2010) 1148–1155. https://doi.org/10.1021/jp910077h

[24] M.E. Baker, Evolution of alpha-fetoprotein: sequence comparisons among AFP species and with albumin species, Tumor Biol. 9 (2–3) (1988) 123–136.

[25] K. Liu, C. Wu, M. Zhu, J. Xu, B. Lin, H. Lin, Z. Liu, M. Li, Structural characteristics of alpha-fetoprotein, including N-glycosylation, metal ion and fatty acid binding sites, Commun. Biol. 7 (2024) 505. https://doi.org/10.1038/s42003-024-06219-0

[26] J.M. Torres, A. Anel, J. Uriel, Alpha-fetoprotein-mediated uptake of fatty acids by human T lymphocytes, J. Cell. Physiol. 150 (3) (1992) 456–462.

[27] J. Nishihira, Y. Koyama, M. Sakai, S. Nishi, The fatty acid binding site of human α-fetoprotein, Biochem. Biophys. Res. Commun. 196 (1993) 1049–1057. https://doi.org/10.1006/bbrc.1993.2357

[28] R.A. Campbell, H.P. Wacklin, I. Sutton, R. Cubitt, G. Fragneto, et al., FIGARO: The new horizontal neutron reflectometer at the ILL, Eur. Phys. J. Plus 126 (11) (2011) 1–22. https://doi.org/10.1140/epjp/i2011-11107-8

[29] H.-y. Tao, R.-q. Wang, W.-j. Sheng, Y.-s. Zhen, The development of human serum albumin-based drugs and relevant fusion proteins for cancer therapy, Int. J. Biol. Macromol. 187 (2021) 24–34.

[30] B. Barletti, N. Paracini, G. Fragneto, J.-P. Alcaraz, A. Nelson, D.K. Vilgrain, Isabelle Martin, M. Maccarini, Glycation enhances protein association with lipid bilayer membranes, Langmuir 41 (46) (2025) 31155–31168.
[31] J.H. Durant, L. Wilkins, J.F.K. Cooper, Optimizing experimental design in neutron reflectometry, Appl. Crystallogr. 55 (4) (2022) 769–781.
[32] J. Penfoldt, R.K. Thomas, The application of the specular reflection of neutrons to the study of surfaces and interfaces, J. Phys. Condens. Matter 2 (1990) 1369–1412.
[33] R.S. Petruzielo, F.A. Heberle, P. Drazba, J. Katsaras, G.W. Feigenson, Phase behavior and domain size in sphingomyelin-containing lipid bilayers, Biochimica et Biophysica Acta (BBA)-Biomembranes 1828 (4) (2013) 1302–1313.
[34] A.I. Greenwood, S. Tristram-Nagle, J.F. Nagle, Partial molecular volumes of lipids and cholesterol, Chem. Phys. Lipids 143 (1-2) (2006) 1–10.
[35] Biomolecular Scattering Length Density Calculator, Accessed: 2020-04-03, http://psldc.isis.rl.ac.uk/Psldc/.
[36] A.R.J. Nelson, S.W. Prescott, Refnx: neutron and X-ray reflectometry analysis in python, J. Appl. Crystallogr. 52 (2019) 193–200. https://doi.org/10.1107/S1600576718017296
[37] O.S. Heavens, Optical properties of thin films, Rep. Prog. Phys. 23 (1) (1960) 1.
[38] L. Nevot, P. Croce, Caractérisation des surfaces par réflexion rasante de rayons X. application à l'étude du polissage de quelques verres silicates, Revue de Physique appliquée 15 (3) (1980) 761–779.
[39] S.B. Nielsen, D.E. Otzen, Quartz crystal microbalances as tools for probing protein-membrane interactions, Methods Mol. Biol. 974 (2013) 1–21.
[40] C.A. Keller, B. Kasemo, Surface specific kinetics of lipid vesicle adsorption measured with a quartz crystal microbalance, Biophys. J. 75 (3) (1998) 1397–1402.
[41] G.J. Hardy, R. Nayak, S. Zauscher, Model cell membranes: techniques to form complex biomimetic supported lipid bilayers via vesicle fusion, Curr. Opin. Colloid Interface Sci. 18 (5) (2013) 448–458. https://doi.org/10.1016/j.cocis.2013.06.004
[42] M.C. Dixon, Quartz crystal microbalance with dissipation monitoring: enabling real-time characterization of biological materials and their interactions, J. Biomolecular Techn. JBT 19 (3) (2008) 151.
[43] M.J. Abraham, T. Murtola, R. Schulz, S. Páll, J.C. Smith, B. Hess, E. Lindahl, GROMACS: High performance molecular simulations through multi-level parallelism from laptops to supercomputers, SoftwareX 1 (2015) 19–25.
[44] J. Lee, X. Cheng, S. Jo, A.D. MacKerell, J.B. Klauda, W. Im, CHARMM-GUI input generator for NAMD, GROMACS, AMBER, OpenMM, and CHARMM/OpenMM simulations using the CHARMM36 additive force field, Biophys. J. 110 (3) (2016) 641a.
[45] J. Huang, S. Rauscher, G. Nawrocki, T. Ran, M. Feig, B.L. De Groot, H. Grubmüller, A.D. MacKerell, Jr, CHARMM36m: an improved force field for folded and intrinsically disordered proteins, Nat. Methods 14 (1) (2017) 71–73.
[46] K.A. Majorek, P.J. Porebski, A. Dayal, M.D. Zimmerman, K. Jablonska, A.J. Stewart, M. Chruszcz, W. Minor, Structural and immunologic characterization of bovine, horse, and rabbit serum albumins, Mol. Immunol. 52 (3–4) (2012) 174–182.
[47] L. Zheng, N. Liu, X. Gao, W. Zhu, K. Liu, C. Wu, R. Yan, J. Zhang, X. Gao, Y. Yao, et al., Uniform thin ice on ultraflat graphene for high-resolution cryo-EM, Nat. Methods 20 (1) (2023) 123–130.
[48] G. Bussi, D. Donadio, M. Parrinello, Canonical sampling through velocity rescaling, J. Chem. Phys. 126 (1) (2007) 014101.
[49] M. Bernetti, G. Bussi, Pressure control using stochastic cell rescaling, J. Chem. Phys. 153 (11) (2020) 114107.
[50] T. Darden, D. York, L. Pedersen, et al., Particle mesh ewald: an N log (n) method for ewald sums in large systems, J. Chem. Phys. 98 (1993) 10089–10089.
[51] N. Michaud-Agrawal, E.J. Denning, T.B. Woolf, O. Beckstein, MDAnalysis: a toolkit for the analysis of molecular dynamics simulations, J. Comput. Chem. 32 (10) (2011) 2319–2327.
[52] P. Smith, C.D. Lorenz, LiPyphilic: a python toolkit for the analysis of lipid membrane simulations, J. Chem. Theory Comput. 17 (9) (2021) 5907–5919.
[53] H.I. Ingólfsson, M.N. Melo, F.J. Van Eerden, C. Arnarez, C.A. Lopez, T.A. Wassenaar, X. Periole, A.H. De Vries, D.P. Tieleman, S.J. Marrink, Lipid organization of the plasma membrane, J. Am. Chem. Soc. 136 (41) (2014) 14554–14559.
[54] R. Richter, A. Mukhopadhyay, A. Brisson, Pathways of lipid vesicle deposition on solid surfaces: a combined QCM-D and AFM study, Biophys. J. 85 (2003) 3035–3047.
[55] R.P. Richter, R. Bérat, A.R. Brisson, Formation of solid-supported lipid bilayers: an integrated view, Langmuir 22 (2006) 3497–3505. https://doi.org/10.1021/la052687c
[56] A. Luchini, S. Micciulla, G. Corucci, K.C. Batchu, A. Santamaria, V. Laux, T. Darwish, R.A. Russell, M. Thepaut, I. Bally, et al., Lipid bilayer degradation induced by SARS-CoV-2 spike protein as revealed by neutron reflectometry, Sci. Rep. 11 (1) (2021) 14867.
[57] N. Paracini, Y. Correa, R.D. Giudice, M. Moulin, H. Pichler, E. Bengtsson, V.T. Forsyth, M.W.A. Skoda, L.A. Clifton, M. Cárdenas, The interaction of human serum components with model membranes containing phospholipids and lipopolysaccharides, J. Colloid Interface Sci. 688 (2025) 150–160. https://doi.org/10.1016/j.jcis.2025.02.131
[58] B. Jachimska, A. Pajor, Physico-chemical characterization of bovine serum albumin in solution and as deposited on surfaces, Bioelectrochemistry 87 (2012) 138–146. https://doi.org/10.1016/j.bioelechem.2011.09.004
[59] J.R. Olivieril, A.F. Craievich, The subdomain structure of human serum albumin in solution under different ph conditions studied by small angle X-ray scattering, Eur. Biophys. J. 24 (2) (1995) 77–84.
[60] R. Kulkarni, E.A.C. Wiemer, W. Chang, Role of lipid rafts in pathogen-host interaction-a mini review, Front. Immunol. 12 (2022) 815020.
[61] I. Ripa, S. Andreu, J.A. López-Guerrero, R. Bello-Morales, Membrane rafts: portals for viral entry, Front. Microbiol. 12 (2021) 631274.
[62] Y. Jiang, B. Thienpont, V. Sapuru, R.K. Hite, J.S. Dittman, J.N. Sturgis, S. Scheuring, Membrane-mediated protein interactions drive membrane protein organization, Nat. Commun. 13 (1) (2022) 7373.
[63] S. Sugio, A. Kashima, S. Mochizuki, M. Noda, K. Kobayashi, Crystal structure of human serum albumin at 2.5 å resolution, Protein Eng. 12 (6) (1999) 439–446.
[64] F. Lolicato, L. Joly, H. Martinez-Seara, G. Fragneto, E. Scoppola, F. Baldelli Bombelli, I. Vattulainen, J. Akola, M. Maccarini, The role of temperature and lipid charge on intake/uptake of cationic gold nanoparticles into lipid bilayers, Small 15 (23) (2019) 1805046. https://doi.org/10.1002/smll.201805046
[65] S. Blaise, H. Polena, I. Vilgrain, Soluble vascular endothelial-cadherin and auto-antibodies to human vascular endothelial-cadherin in human diseases: two new biomarkers of endothelial dysfunction, Vascular Med. 20 (6) (2015) 557–565.
[66] J. Brasch, O.J. Harrison, G. Ahlsen, S.M. Carnally, R.M. Henderson, B. Honig, L. Shapiro, Structure and binding mechanism of vascular endothelial cadherin: a divergent classical cadherin, J. Mol. Biol. 408 (1) (2011) 57–73.